Microstructure evolution and mechanical response of a boron-modified Ti-6Al-4V alloy during high-pressure torsion processing

Shibayan Roy[a,1], Amit Sharma[b,e], Atanu Chaudhuri[b], Yi Huang[c,d], Terence G. Langdon[d], Satyam Suwas[b]

[a] Materials Science Centre, Indian Institute of Technology, Kharagpur, India
[b] Department of Materials Engineering, Indian Institute of Science, Bangalore, India
[c] Department of Design and Engineering, Faculty of Science and Technology, Bournemouth University, Poole, Dorset BH12 5BB, UK
[d] Materials Research Group, Department of Mechanical Engineering, University of Southampton, Southampton SO17 1BJ, UK
[e] Empa, Swiss Federal Laboratories for Materials Science and Technology, Thun, Switzerland

Abstract

Research was conducted on the microstructural evolution and ensuing mechanical response from high-pressure torsion (HPT) processing of Ti-6Al-4V alloy in the as-cast and β-forged conditions with and without 0.1 wt.% boron addition. The boron addition produces refinement of the prior β grains and the (α+β) colonies and introduces an additional TiB phase but this affects the deformation response and the microstructural evolution only at low strains of 0.5 to 5 rotations. In the initial condition the orientation of the (α+β) colonies significantly affects the deformation response and leads to differences in substructure formation in both the as-cast and β-forged conditions. This orientation dependence counts on the initial microstructural differences between the unmodified and the boron modified alloys. At higher strains, there is a similar deformation response and microstructure evolution all the alloys. The hardness variation with equivalent strain is similar for the unmodified and boron modified alloys in as-cast and β-forged conditions and represents various deformation regimes in HPT-processing. Strength modelling confirms a simultaneous contribution from microstructural refinement and increased dislocation density towards the hardness increment during HPT processing. Overall, the as-cast and β-forged Ti-6Al-4V-0.1B alloys possess identical deformation response to the β-forged unmodified Ti-6Al-4V alloy in the initial and intermediate stages. At high levels of straining, all alloys respond in an equivalent manner, thus ruling out any possible effects from additional TiB phase or microstructural refinement for the boron-modified alloys.

Keywords: Ti-6Al-4V alloy, Boron modification; High-pressure torsion; X-ray diffraction line profile analysis; Hardness and strength modeling.

[1] **Corresponding Author: E-mail: shibayan@matsc.iitkgp.ac.in, royshiba@gmail.com, Telephone: +91-3222 283962**

1. Introduction

Two-phase (α+β) titanium alloys such as Ti-6Al-4V are widely used for aerospace, automotive and biomedical applications due to their high specific properties which stems from the low density of Titanium (4.5 gm/cm^3) and excellent corrosion resistance [1] These applications often require a complex design of components which are generally fabricated by expensive machining operations leading to a high wastage of materials [2]. An alternative low-cost solution is the use of near-net-shape casting but then the main difficulty is the coarse microstructure and strong crystallographic texture in the as-solidified condition [3]. A possible breakthrough is the use of a hypoeutectic boron addition of typically ~0.1 wt% which refines the as-cast microstructure by nearly an order of magnitude and weakens the strong solidification texture compared to the unmodified alloy [4]. Boron addition also leads to the formation of TiB particles along prior β grain boundaries during solidification once the eutectic temperature is crossed. This optimized Ti-6Al-4V-0.1B alloy either enhances or maintains most of the mechanical properties of the unmodified alloy in the as-cast condition such as strength, ductility, fatigue and creep resistance [5-8]. The boron-modified alloy also possesses a superior processing response in the β- [9] and (α+β)-phase fields [10, 11-, 12-15] as well as under superplastic conditions [16, 17-19., 18].

Over the last twenty years the use of severe plastic deformation (SPD) processing has emerged as a potential technique for producing ultrafine sub-micrometer grains in bulk solid parts of metals and alloys **[19-24].** Grain refinement in SPD processing occurs through the imposition of a large plastic strain with only a negligible change in the dimensions of the work-piece. Processing by SPD has also proven an effective technique for delineating the deformation response of material systems at high plastic strains which otherwise cannot be achieved in regular mechanical testing [25]. Several SPD techniques have been developed including equal-channel angular pressing (ECAP), accumulative roll bonding (ARB) and high-pressure torsion (HPT) [26-29]. In HPT processing, the work-piece in the form of a thin disk is subjected to a simultaneous high pressure and large shear strain [30, 31]. This has an advantage over ECAP or ARB because it produces smaller grains with higher fractions of high-angle grain boundaries (HAGB) [32, 33].

HPT processing also evolved in recent years as an effective method to produce nano-crystalline materials which are then tested for various properties in order to understand material behavior in the nano-regime. Chen et al. [34] for example refined coarse-grained Ti (average grain

size of ~50 μm) to a nano-structure having an average grain size of ~95 nm by HPT through 10 turns at room temperature. They thereafter studied and compared the fracture behavior of coarse and fine-grained Ti using electrically-assisted micro-tensions through pulsed unidirectional current. Lin et al. [35] similarly deformed commercial purity (CP) Ti and Ti-6Al-4V alloy by HPT for 10 and 20 rotations. Afterwards, they were used to examine the effect of nano-crystalline grains on the surface modification by laser treatment. HPT processing and subsequent annealing were also used to examine the correlation between the microstructure evolution and shape memory response for the Ti-13V-3Al alloy [36]. While HPT introduced high density of defects and decreased the stability of the α″ martensite within the single β phase, annealing at 700°C reintroduced numerous small parallel α″ variants following the residual defects. Among other materials, Anijdan et al. [37] used 6 HPT rotations at a rate of 1 rpm to weaken the texture for Fe-10Ni-7Ms steel and examined the role of dislocation substructure and misoientation formation in the microstructure. Ren et al. [38] similarly examined the role of twin formation and their interaction for rare-earth containing Mg-5.91GD-3.20Y alloy in HPT processing for microstructural evolution and subsequent mechanical response.

Despite significant studies on the thermo-mechanical processing of the Ti-6Al-4V-0.1B alloy there has been no attempt to understand the response of any boron-modified titanium alloys to SPD processing even though these alloys have many potential usages as structural materials. In addition, it is important to note that the TiB-phase in the microstructure of boron-modified alloys was shown to influence almost all mechanical properties including the room temperature tensile [6, 39] and fatigue strengths [7] as well as the deformation response at high temperatures [12, 13-, 14, 15] and under dynamic loading conditions [40]. It is therefore important to evaluate the effect of the secondary TiB-phase on the deformation response of the Ti-6Al-4V-0.1B alloy under extreme straining.

The present research was conducted to systematically evaluate the deformation response of the Ti-6Al-4V-0.1B alloy under SPD conditions. Accordingly, HPT processing was carried out on both an unmodified Ti-6Al-4V alloy and a boron-modified Ti-6Al-4V-0.1B alloy in the as-cast and the β-forged conditions. The β-processing diminishes most of the initial differences, such as microstructural refinement, in the as-cast condition except for the presence of TiB particles in the β-forged Ti-6Al-4V-0.1B alloy [40]. The HPT-processed unmodified and boron-modified alloys were characterized for microstructural evolution using transmission electron

miscopy (TEM), electron backscatter diffraction (EBSD) and X-ray diffraction line profile analysis (XRDLPA). The hardness of the alloys was measured after various HPT rotations. Finally, a microstructure-mechanical property correlation was established from strength modeling which incorporate the contributions from various strengthening mechanisms.

2. Experimental

2.1. Initial materials

Unmodified Ti-6Al-4V (hereafter designated Ti64) and a 0.1 wt% (hypoeutectic) boron-modified Ti-6Al-4V-0.1B (hereafter designated Ti64+B) alloys were used in this study with the chemical compositions given in **Table 1**. The as-cast alloys (hereafter designated Ti64-C and Ti64+B-C, respectively) were prepared by induction skull melting using a graphite mold under identical conditions. Cast ingots were subjected to standard hot isostatic pressing at 900^{o}C and 100 MPa pressure for 2 hours. The β-transus temperature was determined as ~1040^{o}C for the unmodified and ~1020^{o}C for the boron-modified alloys [41]. The as-cast ingots underwent open die forging at 1100^{o}C in the β-phase field at an initial strain rate of 1 s^{-1} and they were then air quenched [40]. The equivalent von Mises strain corresponding to the height reduction in β-forging was 2.48. The β-forged alloys are hereafter denoted as Ti64-F and Ti64+B-F.

2.2. HPT processing

The HPT of the as-cast (Ti64-C and Ti64+B-C) and β-forged (Ti64-F and Ti64+B-F) alloys was conducted at room temperature using circular discs of 10 mm diameter and 1 mm thickness processed through 0.5, 1, 2, 5 and 10 rotations under a speed of 1 rpm at a constant applied pressure of 6.0 GPa. The torsion loading axes were maintained parallel either to the ingot axes for the as-cast alloys or the forging directions for the β-forged alloys. In practice, the imposed equivalent von Mises strain, ε, varies with the distance from the center (r) through the expression [30, 42].

$$\varepsilon = \frac{2\pi r N}{\sqrt{3}h} \quad \ldots\ldots\ldots\ldots\ldots\ldots (1)$$

where N is the number of rotations and h is the thickness of the disc. It follows that ε increases from zero at the center of the disc to a maximum at the edge [42].

2.3. Microstructural characterization

The microstructures of the two starting alloys (Ti64 and Ti64+B) in the as-cast and β-forged conditions were observed using scanning electron microscopy (SEM)[2] in back-scatter electron (BSE) mode. The SEM images were captured from the surfaces perpendicular to the ingot axis in case of the as-cast ingots, thereby also keeping the ingot axis parallel to the image plane normal. For the β-forged alloys the observations were made from the surfaces parallel to the forging direction in the mid-thickness region such that the forging direction lies perpendicular to the image plane normal. The observation surfaces were prepared by metallographic polishing and finished by electro-polishing following the methodology described elsewhere [9-11, 43]. The samples were etched with a custom-made solution containing 5% HF, 10% HNO_3 and water for 30 seconds.

The EBSD scans were captured from the HPT-processed discs for both alloys in the as-cast and β-forged conditions after one rotation where $\varepsilon \approx 25$. The planes parallel to the axis of the HPT discs i.e. normal direction-shear direction (ND-SD) planes near the mid-thickness region and close to the periphery were used for EBSD characterizations (**Supplementary Figure S.1a**). The specimen surfaces were prepared following the same methodology as for SEM without the final etching. The FEG-SEM[3] was operated at an accelerating voltage of 20 kV during the EBSD scans and the orientation data were analyzed using TSL OIM® software considering a minimum boundary misorientation of 2° accounting for the angular resolution of the EBSD technique [44].

The microstructures of the HPT-processed discs from various alloys (unmodified and boron modified in the as-cast and β-forged conditions) after 10-rotations where $\varepsilon \approx 300$ were characterized by TEM in brightfield mode. The TEM[4] was equipped with a field emission source (FEG-TEM) and operated at an accelerating voltage of 300 kV. The TEM specimens were prepared from the ND-SD planes close to the periphery corresponding to the maximum equivalent strain. Further details on the TEM specimen preparation are given in the **Supplementary Section 2**. The average grain sizes for the HPT-processed alloys were calculated from TEM micrographs using the linear intercept method, where the procedure consisted of drawing several horizontal and vertical parallel lines to provide sufficient statistical reliability and covering more than 200 grains for each microstructure.

[2] QUANTA 200, FEI, The Netherlands
[3] FEI SIRION, FEI, Netherlands
[4] FEI Tecnai F-30, FEI, The Netherlands

2.4. X-ray diffraction line profile analysis

The XRDLPA was conducted on the XRD scan data for the HPT-processed discs of the unmodified and boron modified alloys in the as-cast and β-forged conditions. The primary objective was to determine the average crystallite size, the dislocation density, the dislocation arrangement and the average micro-strain as a function of the applied equivalent strain [45]. Thus, XRD patterns were first collected using CuK_{α} ($\lambda = 1.54056$ Å) radiation in a parallel beam optics[5] from the surfaces perpendicular to the axis of the HPT-processed discs and close to the periphery (**Supplementary Figure S.1a**). The X-ray diffractometer was equipped with Johansson optics to eliminate $K_{\alpha 2}$ and K_{β} components from the incident beam. The $\theta - 2\theta$ scans were recorded in a 20°-100° angular range with a scan step of 0.001° and a scan speed of 1°/minute. The XRDLPA was performed following the two methods of conventional Williamson-Hall (W-H) plotting and convolute multiple whole profile (CMWP) fitting where the W-H analysis provides the average crystallite size and micro-strain while CMWP gives the dislocation density and dislocation arrangement within the deformed microstructures [46]. Further details about the classical and modified Williamson-Hall analysis [47-51] and CMWP method [52-54] are provided in **Supplementary Section 3**.

2.5. Hardness measurements for HPT-processed discs

The equivalent von Mises strain (ε) increases from zero at the center of the HPT disc to a maximum at the edge and it also increases with the number of HPT rotations [42]. Hardness measurements were recorded along the diameters on the cross-sectional (ND-SD) planes parallel to the axis of the HPT discs near the mid-thickness regions (**Supplementary Figure S.1b**). An average step size of 0.5 mm was maintained between adjacent indents. Since the HPT discs were processed up to different numbers of HPT rotations, the hardness data provide the variation as a function of imposed equivalent strain (ε) for each alloy. The hardness measurements were recorded using Vickers micro-indentations at a constant normal load of 1000 g and a dwell time of 10 s at peak load. A minimum of five indentations was performed at each location and the average hardness was calculated as the mean with an error given by the standard deviation of the measured dataset.

3. Results

[5]**Rigaku Smartlab, Japan**

3.1. Microstructures of the initial as-cast and β-forged alloys

The microstructures of the unmodified Ti64-C and boron-modified Ti64+B-C alloys in the as-cast condition contain typical Widmänstatten (α+β)-colonies due to the slow/furnace cooling from above the β-phase field (**Figures 1a-b**). The effect of the boron addition and the corresponding microstructural refinement is visible for the Ti64+B-C alloy at different length scales. The prior β-grains are >1000 μm and the (α+β)-colonies are ~300-500 μm for the unmodified Ti64-C alloy whereas for the boron-modified Ti64+B-C alloy these microstructural features are ~200 μm and <50 μm, respectively. Also, the Ti64-C alloy exhibits a thick and continuous grain boundary (GB) α-phase which contrasts with the thin GB α phase or TiB particles lying along the prior β grain boundaries for the Ti64+B-C alloy (**Figure 1b-inset)**. More details on the as-cast microstructure evolution in these alloys are given elsewhere [4, 41].

The β-forged alloys (Ti64-F and Ti64+B-F) show pancake-shaped prior β-grains which are nearly perpendicular to the forging directions (**Figures 1c-d)**. In practice, the identification of prior β-grains is difficult for the β-forged alloys because of the absence of any grain boundary α-phase for both Ti64-F and Ti64+B-F alloys. The TiB particles, which were initially placed at the prior β-boundaries and demarcate the prior β-grains in the as-cast Ti64+B-C alloy, remain present within the prior β-grains and orient along the Hoop or tensile direction in the microstructure of the Ti64+B-F alloy. This suggests that the prior β-grains in the β-forged microstructures are different from those initially present in the as-cast alloy. These β-grains probably form due to dynamic recrystallization during β-forging and then elongate along the secondary Hoop tensile direction on further deformation [9].

It is important to note the measurement of the prior β grain size for the two β-forged alloys (Ti64-F and Ti64+B-F) is difficult because of their elongated, pancake-shaped morphology; statistical reliability is questionable due to a large scatter in the measured datasets. It appears that the width/thickness of the elongated β grains having a wide distribution (50–500 μm) is significantly lower for Ti64-F alloy than the size of the equiaxed β grains (>1000) μm present in the microstructure of the corresponding Ti64-C alloy (comparing Figures 1a with 1c). The boron modified alloys contain comparable sizes for the equiaxed β grains (~200 μm) in Ti64+B-F alloy and the width/thickness of elongated β grains for the Ti64B-F alloy. Due to the difficulty in the identification of prior β grains, particularly in the length direction, no quantitative comparison is possible between the as-cast and corresponding β-forged alloys irrespective of unmodified or boron modified conditions.

The α-phase morphology also changes from lamellar in the as-cast alloys (Ti64-C and Ti64+B-C) to acicular forming a basket-weave microstructure after β-forging for the Ti64-F and Ti64+B-F alloys. The microstructure of the Ti64-F alloy also appears refined in terms of the (α+β)-colonies as well as α-lamellae compared to the corresponding as-cast alloy (Ti64-C). For the boron-modified alloy there is little further microstructural refinement after β-forging (Ti64+B-F) from the as-cast condition (Ti64+B-C). More details on the microstructures of the β-forged alloys (Ti64-F and Ti64+B-F) are given elsewhere [40].

3.2. Microstructure evolution at low strains in HPT processing

Figures 1a-d represent the normal direction inverse pole figure (ND-IPF) maps overlaid with image quality (IQ) for the unmodified and boron-modified alloys in the as-cast and β-forged conditions after one HPT rotation where $\varepsilon \approx 25$. The EBSD data were appropriately rotated so that ND in the IPF maps coincides with the normal of the HPT discs. The misorientation variations along a line are plotted on a point-to-point and point-to-origin basis from selected microstructural regions. The point-to-origin misorientation compares the orientation of each pixel with the starting point (origin) while the point-to-point misorientation compares with the immediate previous pixel [55]. It is important to note that the variation in misorientation within 1-2^{o} is below the resolution limit of the EBSD technique [44] and should be ignored. The standard stereographic triangle superimposed with reference color triangle for hcp materials is provided in **Supplementary Section 4** which represents important directions and corresponding reference colors in EBSD IPF maps

3.2.1. As-cast alloys

After one HPT rotation the as-cast Ti64-C alloy showed several (α+β)-colonies having directions $< 11\bar{2}0 >/< 10\bar{1}0>$ parallel or closely aligned to the HPT disc normal (represented by green and blue colors, respectively, in the IPF map, **Figure 2a:left**). Most of these (α+β)-colonies retain lamellar morphologies without any sign of fragmentation. Some (α+β)-colonies having $< 10\bar{1}1 >/< 10\bar{1}2 >/< 2\bar{1}\bar{1}4 >$ directions parallel to ND (represented by purple or magenta or yellow colors, respectively, in the IPF map) show indications of fragmentation after the HPT processing. The EBSD microstructure also contains certain regions of poor image quality plus high densities of non-indexed pixels which appear black in the overlaid IQ map. These areas correspond to extreme strain accumulations during the HPT processing where this is most probably due to shear band formation [56, 57]. In addition, one of the (α+β)-colonies

with an original orientation close to $ND||<10\bar{1}0>$ appears bent and forms a kinked morphology enclosed by the red dotted line in the HPT microstructure. In another instance, a macroscopic shear band runs through the kinked (α+β)-colony (marked by a white dotted line), thereby separating it into two parts having orientations $ND||<10\bar{1}0>$ (color blue/aqua) on the left and $ND||<2\bar{1}\bar{1}4>$ (color yellow/orange) on the right.

Misorientation variations are plotted on a point-to-point and point-to-origin basis through the (α+β)-colonies (**Figure 2a:right)** having orientations of (1) $<4\bar{1}\bar{3}6>$||ND (line 1) and (2) ND||$<11\bar{2}0>$ (line 2). For both lines 1 & 2, the point-to-point misorientations between adjacent pixels are within 1–2^o with occasional spikes as high as 5^o and even rarely to 8–10^o. The point-to-origin misorientations vary significantly between the two lines. Thus, for line 1 there is a continuous buildup of misorientation with distance from the origin reaching as high as ~25–30^o which is in sharp contrast to the corresponding point-to-point misorientation variation. For line 2 the point-to-origin misorientation shows no continuous buildup with distance but rather stays within 10–15^o to the origin but with spikes at locations identical to the corresponding point-to-point misorientation variations.

The lamellar morphology for (α+β)-colonies are not well preserved and the α-grains are fragmented at several locations for the Ti64+B-C alloy after one HPT rotation (**Figure 2b:left)**. This holds irrespective of the (α+β)-colony orientations of $ND||<11\bar{2}0>/<10\bar{1}0>$ and $ND||<4\bar{1}\bar{3}6>/<10\bar{1}2>/<2\bar{1}\bar{1}2>$. Similar to the Ti64-C alloy, the EBSD microstructure for the Ti64+B-C alloy contains regions of poor image quality indicative of strain accumulation by shear band formation [56, 57]. Misorientations are again plotted on a point-to-point and point–to-origin basis through two different (α+β)-colonies (**Figure 2b:right)**: (1) line 1 through $ND||<11\bar{2}0>$ and then $ND||<10\bar{1}0>$ and (2) line 2 through $ND||<2\bar{1}\bar{1}2>$ and then $ND||<10\bar{1}2>$ orientations. The point-to-point misorientations show nearly similar variations for the two lines with average misorientations within 1–2^o and occasional spikes reaching 5–6^o. The point-to-origin misorientation variations also show sharp differences between the two lines. Thus, for line 1 the misorientation continuously builds up with distance and reaches as high as ~10–12^o. For line 2 two different regimes are separated by a sudden jump of ~20^o that corresponds to the change of orientation from $ND||<11\bar{2}0>$ to $ND||<10\bar{1}0>$. It is important to note that if these two regimes are considered separately the point-to-origin misorientation variation along line 2 should also represent a continuous misorientation buildup of as much as ~5^o with distance from the origin.

3.2.2. β-forged alloys

Concerning the two β-forged alloys, the EBSD microstructure for the Ti64-F alloy contained a single α-grain with $ND||<11\bar{2}0>$ orientation after one HPT rotation (**Figure 2c:left**). This α-grain contained a few parallel band-like regions of poor image quality, marked by white arrows, which are ~1–2 μm in width and separated by an average distance of 15–20 μm. They are probably micro-shear bands from the HPT processing signifying extreme strain localization within this α-grain [57]. The point-to-point and point-to-origin misorientations parallel to these shear bands exhibit similar variations characterized by spikes at frequent intervals (**Figure 2c:right)**. For the point-to-point misorientation these spikes are within 5–7° whereas for the point-to-origin misorientation they often reach to 15–25°. By contrast, the Ti64+B-F alloy consisted of broken α-grains plus remnants of the original α-lamellae having $ND||<11\bar{2}0>$ orientation in the EBSD microstructure after one HPT rotation (**Figure 2d:left)**. Here again there are regions of poor image quality indicating strain accumulation due to shear band formation [56, 57]. The point-to-point misorientation through the lamellar α regions represent the usual variation with an average misorientation of 1–2° and occasional spikes reaching 5–7° (**Figure 2d:right)**. The point-to-origin misorientation increases continuously with distance up to a maximum of ~15° for this alloy and the misorientation occasionally drops within ~2°.

3.3. Microstructure evolution after extreme straining in HPT processing

3.3.1. As-cast alloys

The microstructures for the as-cast alloys (Ti64-C, **Figure 3** and Ti64+B-C, **Figure 4**) subjected to 10 HPT rotations contain α-grains of equivalent sizes of <50 nm in the respective TEM micrographs even though the corresponding (α+β)-colony sizes differ by almost an order of magnitude (**Figures 1a-b)**. For the Ti64-C alloy, the microstructure remains quite homogenous and uniform after HPT processing**.** The heterogeneous contrast within a single grain in the case of any deformed material is generally caused by the presence of defects e.g. dislocations; the higher the dislocation density so the darker is the contrast [58]. The lighter contrast within most of the α-grains therefore indicates a lower defect density and an absence of dislocation substructure for Ti64-C alloy after HPT processing for 10 rotations. High magnification TEM images from selected regions of **Figure 3a** further display microstructural features which are characteristics of SPD processing [27-30]. Certain α grains for example contain dislocation cells (DC) which are prominent from alternating darker and brighter

contrast (Figure 3a-inset, right-top) **[59, 60].** These substructural features almost certainly form out of the dislocation tangled zones (DTZ) by dynamic recovery through annihilation and rearrangement of dislocations during the HPT processing [31, 61-65]. The corresponding selected area diffraction (SAD) pattern presents only an HCP α-phase without any indication of a strain-induced phase transformation even after large straining ($\varepsilon \approx 300$) (**Figure 3a-inset, right-bottom)** [66]. Additionally, semi-continuous rings in the SAD pattern suggest nanocrystalline α-grains and a large fraction of high-angle grain boundaries (HAGBs) in the deformed microstructure of the Ti64-C alloys after 10 HPT rotations.

For certain α grains, relatively darker contrast near the grain boundary regions again indicates higher dislocation density compared to the α grain interiors which mainly consist of dislocation cells (marked in Figure 3b). Some sections of these grain boundary (indicated by white dots) are hard to determine and not well developed; they possibly represent low angle grain boundary (LAGB, misorientation $<15^{o}$) [58]). On the other hand, the grain boundary segments (indicated by red arrows) are well developed and sharp and are as such characteristics of high angle grain boundary (HAGB). Such wavy, non-distinct LAGBs are typical of the high-energy non-equilibrium boundaries reported after HPT processing of various metals and alloys using high-resolution TEM [68].

The microstructure of the boron-modified as-cast Ti64+B-C alloy after 10 HPT rotations was again relatively homogeneous and similar to the as-cast Ti64-C alloy. **Figure 4a** shows certain regions contaning dislocation cell (DC) structures (identified by alternating darker and brighter contrast) within the microstructure. It also exhibited a few elongated non-fragmented α-grains (highlighted in **Figure 4a-inset**) and a lower defect density within most of the α-grains. The corresponding high magnification TEM image (**Figure 4b)** shows a few strain-free α-grains together with regions of higher dislocation density. Inside the α-grains, parallel dislocations reveal band contrast imaging (BCI) patterns. These patterns are formed from the overlapping strain fields of dislocations, possibly having parallel Burger vectors oriented at a certain angle to the electron beam [69]. The microstructures for the two as-cast alloys are therefore quite similar after large straining to $\varepsilon \approx 300$ suggesting that their initial microstructural differences due to the boron addition are probably mitigated under extreme straining in HPT processing.

3.3.2. β-forged alloys

For the β-forged Ti64-F alloy a low magnification TEM image (**Figure 5a)** displayed a heterogeneous microstructure having irregular morphology for most of the α-grains after 10 HPT rotations. A large fraction of these grain boundaries appears wavy and non-distinct which is a characteristic of SPD processing [31, 61-63, 65, 67, 68]. As with the as-cast Ti64-C alloy, the SAD pattern confirms the presence of only the HCP α-phase for the Ti64-F alloy without any strain-induced phase transformation (**Figure 5a-inset)**. The semi-continuous diffraction rings indicate nano-crystalline α-grains and HAGBs after 10 HPT rotations. The microstructure also shows remnants of elongated α-grains (indicated by yellow arrows) plus equiaxed α-grains (marked by white dotted lines in Figure 5b). The latter may have formed from fragmentation of the elongated α-grains. The equiaxed α-grains also contain dislocation cell (DC) and other substructure features (Figure 5b-inset).

The Ti64+B-F alloy similarly exhibits considerable heterogeneity in the microstructure after 10 HPT rotations. It contains a high fraction of equiaxed α-grains (indicated by red arrows) in addition to some elongated α-grains (indicated by dotted rectangle in **Figure 6a)**. There are also some fragmented equiaxed α-grains within the elongated α-grains. The SAD pattern confirms the presence of a single HCP α-phase after 10 HPT rotations **(Figure 6a-inset)**. The high magnification TEM image in Figure 6b further display a BCI pattern (indicated by yellow arrows) with alternating black and grey bands within the elongated α-grains. In addition, deformation bands characterized by alternating black and grey contrasts are present in the microstructure with sharp parallel boundaries (indicated by black and white arrows in Figure 6b-inset). These bands represent heterogeneous contrast due to the accumulation of large quantities of dislocations. The heterogeneous contrast and especially the BCI pattern indicate a high defect density in the microstructure due to the large imposed strain of $\varepsilon \approx 300$ [69]. Overall, the extreme straining to 10 HPT rotations leads to an equivalent microstructure for the β-forged unmodified and boron-modified alloys as with the corresponding as-cast alloys. This further suggests a minimal influence from the TiB-particles during HPT deformation of the boron-modified alloys.

3.4. X-ray diffraction line profile analysis (XRDLPA)

The average crystallite size and microstrain determined from the Williamson-Hall plots (**Supplementary Figure S.3**) are represented in **Figure 7**. Details about the Williamson-Hall method are given in **Supplementary Section 3.1**. [48, 70]. The Ti64-C alloy has the highest crystallite size after 0.5 rotation which is drastically reduced after 5 and 10 HPT rotations. The

other alloys of Ti64+B-C, Ti64-F and Ti64+B-F also follow a similar reduction in crystallite size with increasing HPT rotations. This reduction is quite gradual and nearly linear for the β-forged alloys (Ti64-F and Ti64+B-F) compared to the as-cast alloys (Ti64-C and Ti64+B-C) and most of the reduction in the as-cast alloys occurs within 5 HPT rotations. The extent of microstructural refinement is a minimum for the Ti64+B-F alloy where the crystallite size is 15.1 nm after 10 HPT rotations. This contrasts with the other three alloys (Ti64-C, Ti64+B-C and Ti64-F) where HPT processing to 10 rotations reduces the crystallite size to within 11.5–12 nm.

The micro-strain calculated from the Williamson-Hall plots increases with the numbers of HPT rotations for both alloys irrespective of the initial condition. For the Ti64-C alloy the increase is moderate after 0.5 to 5 rotations and further up to 10 rotations whereas it is quite steep initially for the Ti64+B-C alloy between 0.5 to 5 rotations but saturates afterwards up to 10 rotations. Of the two β-forged alloys, the micro-strain increases almost linearly with the number of HPT rotations for the Ti64-F alloy while the Ti64+B-F alloy shows a significant increase in micro-strain only after 5 rotations but thereafter exhibits a decrease after 10 rotations. Overall, the micro-strain remains the lowest for the Ti64-C alloy and similar (~1.1–1.2%) for the other three alloys after 10 rotations.

Further insight into the dislocation substructure evolution during HPT processing may be obtained from the CMWP analysis. The calculations measure the variations in different parameters (e.g. area average crystallite size, $< x >_{\text{avg}}$, dislocation density, ρ, effective core cut-off radius, R_e and dislocation arrangement parameter, M) with increasing strain [46]. More details about the CMWP method as well as the corresponding XRD fitting plots after 0.5, 5 and 10 HPT rotations for various alloys are given in **Supplementary Section 3.2**. The difference between the experimentally captured and the CMWP-fitted patterns (shown in the insets of **Supplementary Figures S.4a-f**) indicates reasonably good fittings for both the unmodified and boron modified alloys in the as-cast and β-forged conditions. As with the Williamson-Hall analysis, the general observation from CMWP is that the area average crystallite size ($< x >_{\text{avg}}$) decreases and the dislocation density (ρ) increases with equivalent strain, ε, for all alloys (**Figures 8a-d**). The crystallite size variation with equivalent strain is also reasonably similar irrespective of the boron addition or β-forging. In practice, there are two regions with nearly linear variations in each segment. In the initial region up to $\varepsilon \approx 50$ the crystallite size decreases acutely but then saturates with increasing equivalent strain up to 10

HPT rotations. The increase in dislocation density with equivalent strain is fairly linear for the Ti64+B-C and Ti64-F alloys throughout the course of the HPT processing. For the Ti64-C and Ti64+B-F alloys the ρ vs. ε plots again show two different regions with both regions characterized by nearly linear variations but the initial increase is quite sharp up to $\varepsilon \approx 50$ and the slope decreases thereafter up to 10 HPT rotations.

3.5. Hardness variation in HPT processing

Figure 9 shows the hardness variation with increasing equivalent strain (ε) for the unmodified and boron-modified alloys in the as-cast and β-forged conditions. Also shown is the range of equivalent strains encountered after various HPT rotations. The hardness variations contain distinct regions in terms of equivalent strains for all alloys irrespective of the boron addition or β-forging. Thus, the hardness initially increases for the four alloys almost linearly with equivalent strain up to $\varepsilon \approx 20 - 25$ following a steep slope. With further increase in strain up to $\varepsilon \approx 50 - 60$ the hardness varies with a gradually decreasing slope and then the hardness variation with equivalent strain saturates to a near steady state as in the Ti64-C and Ti64+B-C alloys or increases at a smaller slope as in the Ti64-F and Ti64+B-F alloys. The transition in hardness variation from an initial higher slope to a near steady state occurs within $\varepsilon \approx 20 - 60$ for all alloys that form saddle regions irrespective of the boron addition or β-forging. It is noted that a continuous increase in hardness without saturation even after 10 HPT rotations was reported previously for HPT-processed copper [71], for the ZK60A magnesium alloy [72] and for the Ti-6Al-4V alloy [73]. A similar trend was observed in the present study only for the two β-forged alloys of Ti64-F and Ti64+B-F although at a much lower rate.

Although the initial hardness of the alloys are similar at ~300 Hv irrespective of the boron addition or β-forging, a significant difference occurs near the transition regions of $\varepsilon \approx 20 - 60$ as well as towards the end of HPT processing at $\varepsilon \approx 250$. The unmodified β-forged alloy (Ti64-F) continues to have the highest hardness among all the alloys after the transition region and up to the end. For the boron-modified alloys such as Ti64+B-C and Ti64+B-F the hardness is lower in the transition region than for the two unmodified alloys of Ti64-C and Ti64-F. The relatively lower hardness continues for the Ti64+B-C alloy until the end of HPT processing but the lower hardness mitigates for the Ti64+B-F alloy up to $\varepsilon \approx 150$ and thereafter the hardness of this alloy continues to be higher than for the Ti64-C alloy.

4. Discussion

4.1. Microstructure evolution during HPT-processing

4.1.1. The low strain regime

HPT processing produces a significantly different microstructure evolution for the unmodified and boron modified alloys at lower equivalent strains. Thus, while the unmodified Ti64-C alloy presents a homogeneous microstructure with a pronounced dislocation substructure formation, the Ti64+B-C alloy is characterized by deformation inhomeginities as micro-bands. Even when the starting microstructures are similar in the β-forged condition, deformation heterogeneities set in easily for the Ti64+B-F alloy during HPT-processing. The orientation of the (α+β)-colonies significantly influences the deformation response and the resultant substructure evolution at lower equivalent strains. This is evident from the similarities and differences in the misorientations on point-to-origin and point-to-point bases that indirectly represent the dislocation sub-structure evolution for the two alloys in the as-cast or β-forged conditions.

4.1.1.1. Orientation dependency of the substructure evolution

When the two misorientation bases (point-to-origin vs. point-to-point) contain significant differences (e.g. the point-to-point misorientation shows occasional spikes while the point-to-origin continuously increases from the origin), it suggests a misorientation build up via a subtle additive process in absence of any dislocation substructure formation within the α-grains [74]. The deforming (α+β)-colony in this case possibly accommodates the imposed deformation by micro-band formation without the development of any macroscopic instability [75]. These micro-bands may lead to continuous orientation alternations within the relevant (α+β)-colony leading to an increase in the point-to-origin misorientation with distance [55]. On the other hand, a similarity in the point-to-origin and point-to-point misorientation variations with distance (e.g. occasional spikes without a continuous misorientation buildup) indicates well-defined sub-grain formation within the α-grains [76]. In the present experiments, occasional spikes represent sub-grain boundaries while the low misorientation regions correspond to interiors with relatively fewer dislocations [55, 77].

Comparing the two misorientation bases (point-to-origin vs. point-to-point, **Figures 2a-d**), it appears that the (α+β)-colonies with $ND||<11\bar{2}0>/<10\bar{1}0>$ orientations are prone to subgrain formation for the unmodified alloy in the as-cast (Ti64-C, line 2) and β-forged (Ti64-F) conditions. These α grains are probably easy orientations for slip activation and therefore they deform via dislocation activities. In addition, they are prone to macroscopic shear band

formation as is prominent for the β-forged Ti64-F alloy and, to a lesser extent, for the as-cast Ti64-C alloy. It was argued that macroscopic shear bands are favored from the presence of subgrains which effectively hinder the homogeneous glide of sessile dislocations during further straining and localize the deformation in the form of intense shear bands [78]. For boron-added alloys (Ti64+B-C, line 2 and Ti64+B-F), (α+β)-colonies with $ND||<11\bar{2}0>/<10\bar{1}0>$ orientations do not favor subgrain formation by dislocation activities and instead they deform primarily by micro-band formation as is evident in the continuous misorientation build up in the point-to-origin basis. Thus, they are possibly hard orientations under shear deformation in HPT-processing [10, 43]. Furthermore, the (α+β)-colonies with $ND||<4\bar{1}\bar{3}6>/<10\bar{1}2>/<2\bar{1}\bar{1}2>$ orientations represents continuous misorientation buildup in point-to-origin basis for unmodified (Ti64-C, line 1) as well as boron modified alloys (Ti64+B-C, line 1) in the as-cast condition. This suggests that for both the unmodified and boron modified alloys this orientation is not favorable for subgrain formation and therefore these are hard orientations that promote micro-band formation [10, 43].

It is interesting to note that under uniaxial loading (tension or compression), $ND||<11\bar{2}0>$ and $ND||<10\bar{1}0>$ act as hard orientations since the Schmidt factor is zero for both basal and prism $<a>$ slip since the slip plane and slip direction, respectively are parallel to the straining direction [12, 43, 79]. On the other hand, the $ND||<4\bar{1}\bar{3}6>/<10\bar{1}2>/<2\bar{1}\bar{1}2>$ orientations favor multiple slip and as such these are soft orientations under uniaxial loading since the Schmidt factor is non-zero for both basal and prism $<a>$ slip. The orientation dependency of the slip activation is thus somewhat reversed under shear deformation in HPT-processing in contrast to uniaxial (tension or compression) loading. This occurs since the shear stresses in torsion can make the Schmidt factor non-zero for basal and prism $<a>$ slip even in the case of $ND||<11\bar{2}0>/<10\bar{1}0>$ orientations [80]. In addition, the applied shear stresses vary in magnitude and direction over the HPT discs so that it may further add to the complexity of the orientation dependence of the slip activation and the dislocation sub-structure evolution [30]. The $ND||<11\bar{2}0>/<10\bar{1}0>$ orientation therefore deforms under considerable dislocation activities and may eventually contain sub-grains after one HPT rotation. Similarly, shear deformation may reduce the propensity for multiple slip and subgrain formation in the $ND||<4\bar{1}\bar{3}6>/<10\bar{1}2>/<2\bar{1}\bar{1}2>$ orientations, and rather may promote a continuous misorientation buildup due to micro-banding. Any further discussion about the

orientation dependency of the slip activation under shear (torsional) loading and the subsequent substructure formation during HPT-processing is beyond the scope of the present work.

4.1.1.2. Effect of starting microstructure on substructure evolution

The orientation dependency of the slip activation and the resultant sub-structure formation is quite different between the unmodified and boron modified alloys. For example, the $ND||<10\bar{1}0>/<11\bar{2}0>$ orientations lead to subgrain formation and macroscopic shear banding for the unmodified as-cast or β-forged alloys whereas the $ND||<4\bar{1}\bar{3}6>/<10\bar{1}2>/<2\bar{1}\bar{1}2>$ orientations deform by micro-banding accompanied by a gradual change in misorientation without substructure formation (**Figures 2a-d**). The boron modified alloys in the as-cast and β-forged conditions always exhibit micro-banding irrespective of their oorientations ($ND||<10\bar{1}0>/<11\bar{2}0>$ or $ND||<4\bar{1}\bar{3}6>/<10\bar{1}2>/<2\bar{1}\bar{1}2>$). Thus, while subgrain formation occurs for certain orientations in the unmodified alloy, micro-banding always dominates for the boron-modified alloy. These differences are quite prominent in the as-cast alloys but are mitigated after β-forging and this is probably related to the initial microstructural differences that influence slip activation and the deformation responses during HPT-processing.

The as-cast microstructure for Ti64+B-C differs from Ti64-C in terms of a smaller (α+β)-colony, a low aspect ratio for α-lamellae plus a higher number of α-variants within the prior β-grains [4]. These differences in turn ensure a higher proportion of α/β-interfaces for the Ti64+B-C alloy and may lead to a higher possibility of dislocation pile ups (similar to Hall-Petch strengthening) either at (α+β)-colony boundaries or at α/β interphase boundaries during deformation and slip transfer [10, 81]. In addition, brittle TiB particles can accumulate strain due to a deformation mismatch with the ductile α/β matrix [14]. In turn, the deformation inhomogeneities leading to substantial flow localization (i.e. micro-bands) are easy to set up for the boron-modified alloy compared to the unmodified alloy [12]. HPT-processing therefore can produce an additive misorientation development and an absence of subgrains irrespective of the α phase orientations for the boron modified alloys in the as-cast and β-forged conditions. Most of the initial microstructural differences in the as-cast condition between the unmodified and boron-modified alloys (e.g. (α+β)-colonies or α-lamellae sizes) are mitigated after β-forging [40] so that the only remaining difference relates to the TiB-particles within the prior β-grains. The formation of a deformation inhomogeneity from dislocation pile-ups is therefore equally likely for the two alloys in the β-forged condition. This possibly produces a minimal

difference in substructure evolution for the $ND||<11\bar{2}0>/<10\bar{1}0>$ orientations between the two alloys. Whatever little differences still persists can therefore be attributed to the strain accumulation at TiB-particle sites in the case of the Ti64+B-F alloy irrespective of the (α+β)-colony orientations.

For further insights regarding the substructure evolution in the low strain regime, the dislocation arrangement parameter, $M = R_e * \sqrt{\rho}$, can be considered for different HPT-rotations as shown in **Table 2**. This parameter is determined from a CMWP analysis considering the corresponding dislocation density (ρ) and effective cut-off radius (R_e). Thus, the value of M denotes the arrangement of dislocations and their interaction with strain fields [46, 54]. A value of $M > 1$ represents a quite random arrangement of dislocations whereas for $M < 1$ the dislocations are perfectly ordered [82]. In practice $M > 1$ occurs only for the Ti64-F alloy irrespective of the number of HPT rotations suggesting a weak correlation between the dislocations probably due to the inhomogeneous deformation as micro- or macroscopic shear bands. This prediction is in line with the corresponding EBSD observations (**Section 3.2**, **Figure 2a**). For the Ti64-C alloy, $M << 1$ indicates an ordered dislocation arrangement, probably as a well-defined substructure after HPT-processing. This prediction again corroborates well with the EBSD results wherein (α+β)-colonies with $ND||<11\bar{2}0>/<10\bar{1}0>$ orientations form subgrains after one HPT rotation. For the boron modified alloys (Ti64+B-C and Ti64+B-F), $M < 1$ (but higher than M for the Ti64-C alloy) and this possibly represents an intermediate microstructure characterized by both inhomogeneous deformation (micro-bands) and dislocation substructure formation. This again supports the corresponding EBSD observations that boron modified alloys primarily deform by micro-band formation irrespective of α-grain orientation and to a limited extent by subgrain formation during the initial part of HPT-processing.

4.1.2. After extreme straining

Unlike the lower equivalent strain regime, the microstructure evolution are quite similar after large straining up to 10 HPT-rotation for the unmodified and boron modified alloys in the as-cast and β-forged conditions. One noticeable difference is that, whereas homogeneous microstructures prevail after HPT-processing of the as-cast alloys, relatively heterogeneous microstructures evolve in the β-forged alloys. The common microstructural features for all HPT-processed alloys are nano-crystalline, defect-free equiaxed α-grains surrounded by

HAGBs plus a few elongated α-grains and regions of high defect density. These features are characteristic of SPD processing including for HPT of pure titanium [61] as well as titanium alloys [62, 63, 65]. The average crystallite size and the micro-strain or dislocation density obtained from XRDLPA are also quite similar for all alloys after extreme straining. This suggests that the starting differences due to the boron addition (for example, the microstructural refinement or TiB phase formation) do not significantly influence the microstructure evolution after extreme straining ($\varepsilon \approx 300$).

In order to understand the pathway of microstructure evolution in HPT-processing, from a homogeneous microstructure with pronounced dislocation substructure at the lower strain regime to a homogeneous nanostructure at extreme straining for the Ti64-C alloy, the XRDLPA results can be further examined. The change in dislocation density and crystallite size with number of HPT rotations is different for the unmodified and boron-modified alloys or between their initial conditions (as-cast vs. β-forged). For example, the decrease in crystallite size (**Figure 7e**) or increase in dislocation density (**Figure 8**) with increasing equivalent strain is gradual for the boron-modified Ti64+B-C or Ti64+B-F alloys as well as for the unmodified Ti64-F alloy. On the contrary, the decrease in crystallite size or the increase in dislocation density between 0.5 to 5 HPT rotations are quite drastic for the unmodified Ti64-C alloy which thereafter saturates with increasing equivalent strain up to 10 HPT rotations. This difference in the substructure evolution is probably related to the starting microstructural differences between the various alloys.

The coarse as-cast microstructure for the Ti64-C alloy promotes homogeneous deformation without effective dislocation pile ups during the initial part (as also explained in **Section 3.2**) and this may cause fragmentation of the α-lamellae from sub-grain formation only after substantial straining up to 5 rotations and continues thereafter to 10 rotations. This can in turn produce a drastic decrease in the crystallite size and an increase in the dislocation density initially between 0.5 to 5 rotations [45, 70]. Continued fragmentation at a steady rate may further cause the dislocation density and crystallite size to nearly saturate between 5 and 10 rotations. The other three alloys (Ti64-F, Ti64+B-C and Ti64+B-F) contain almost equivalent refined microstructures at the beginning due to either the boron addition or β-forging. For these alloys, inhomogeneous deformation is then characterized by significant dislocation pile up at the lower strain levels. The α-lamellae fragmentation therefore can occur even within 0.5 rotation and continue with increasing equivalent strain up to 5 and 10 rotations.

4.2. Strength modeling for a structure-property correlation

The variation in hardness with imposed equivalent strain for the two alloys (unmodified and boron-modified) in different starting conditions (as-cast and β-forged) carries the signature of the characteristics of microstructure and sub-structure evolution in HPT-processing. The hardness remains the highest for the Ti64-F alloy and the lowest for the Ti64+B-C alloy throughout the course of HPT processing, and at the highest strain ($\varepsilon \approx 225$) it is ~395 Hv and ~365 Hv, respectively. The higher hardness for the Ti64-F alloy is attributed to the very significant microstructural refinement induced by HPT processing. The starting microstructure of Ti64-F possesses a basket-weave structure with fine acicular α-lamellae which contribute to the rapid fragmentation during HPT-processing [81]. Due to the similar microstructural refinement and fine acicular α-lamellae, the Ti64+B-F alloy also exhibits a substantial increase in hardness after the transition region towards the end of the HPT-processing. The as-cast Ti64-C and Ti64+B-C alloys with initial coarse lamellar (α+β) colonies undego microstructural fragmentation at a reduced rate in the HPT processing leading to a steady-state hardness variation with increasing equivalent strain beyond the transition regions.

To further ascertain the correlation between the micro/sub-structure evolution and the mechanical properties, a strength modeling approach is now developed. The primary mechanisms of the strength or hardness increment are Hall-Petch strengthening due to the microstructural refinement and Taylor strengthening from the increase in the dislocation density. The details of the strength modeling are provided in **Supplementary Section 5**. Assuming a linear summation of the individual contributions, the calculated strength ($\sigma_{\text{calculated}}$) is represented as [83]:

$$\sigma_{\text{calculated}} = \sigma_o + \Delta\sigma_{\text{Taylor}} + \Delta\sigma_{\text{Hall-Petch}} = \sigma_o + \alpha GMb\sqrt{\rho} + \frac{K}{\sqrt{d}} \quad \ldots\ldots\ldots\ldots (2)$$

The strength modeling is carried out considering only Hall-Patch strengthening ($\Delta\sigma_{\text{Hall-Petch}}$) and Taylor strengthening ($\Delta\sigma_{\text{Taylor}}$) and with a linear summation of both strengthening models as given in **Equation 2**. **Figures 10a-d** present a comparison between the measured and the calculated strengths (σ_{measured} vs. $\sigma_{\text{calculated}}$) at different equivalent strains with the embedded straight lines denoting a perfect match ($\sigma_{\text{measured}}/\sigma_{\text{calculated}} = 1$) between them.

When considering only Hall-Petch strenthening, the best match (from least square fitting) between σ_{measured} and $\sigma_{\text{calculated}}$ corrospond to a Hall-Petch constant, $K \approx 3200$ MPa nm$^{-1/2}$

for the unmodified Ti64-C as well as the boron-modified Ti64+B-C and Ti64+B-F alloys and ~2850 MPa $nm^{-1/2}$ for the unmodified Ti64-F alloy. In this condition, $\sigma_{calculated}$ largely underestimates $\sigma_{measured}$ at all equivalent strains irrespective of the boron addition or β-forging. The deviation at lower equivalent strains suggests that dislocation or Taylor strenthening is active from the beginning of the HPT processing and this is also supported from the EBSD results after one HPT rotation (**Section 3.2**). A similar deviation after large straining, however, indicates that microstructural refinement or nano-crystalline α-grain formation is insufficient to fully account for the strength increment for the HPT-processed alloys because of the presence of a large fraction of dislocation substructure.

By contrast, when considering only dislocation or Taylor strengthening, the best matches between $\sigma_{measured}$ and $\sigma_{calculated}$ are obtained for α values in the range of ~1.0-2.0 which is higher than reported previously [84]. The $\sigma_{calculated}$ in this case underestimates $\sigma_{measured}$ in lower equivalent strain regime up to $\varepsilon \approx 100$ but somewhat overestimates at further higher equivalent strains. The underestimation again implies that dislocation substructure formation cannot fully justify the strength increment alone for the various HPT-processed alloys. Similarly, the overestimation of the measured strength at higher equivalent strains indicates that the calculated α values are errorneous and should be modified to correspond to the form of the dislocation substructure evolution. Overall, Taylor strengthening alone leads to a reasonable prediction of strength inrement compared to only Hall-Petch strengthening. This is also appearant from the extent of the under or overestimatrions with respect to the perfect linear match between $\sigma_{measured}$ and $\sigma_{calculated}$. Thus, Taylor strentheing alone predicts a strength increment closer to the linear match while Hall-Petch strenthening alone predicts a strength increment that is far removed from a linear match.

These contributions should be considered together since HPT processing imparts extreme equivalent strains and leads to significant microstructural refinement as well as a large dislocation density. In the linear summation approach, microstructural refinement (Hall-Petch) and dislocation (Taylor) strengthening were selected for a best fitting between $\sigma_{measured}$ and $\sigma_{calculated}$ by optimizing α and K using the Marquard-Levenberg non-linear fitting. The values of K and α were determined as ~2400-3200 $MPam^{-1/2}$ and ~0.1-0.5, respectively, and these values are within the range for SPD-processed titanium and titanium alloys [85]. A good match is obtained between $\sigma_{measured}$ and $\sigma_{calculated}$ at all equivalent strains suggesting that a combination of Hall-Petch and Taylor strengthening is effective for estimating the strength

increment of the HPT-processed alloys. This is also in agreement with previous strength modeling of nanostructured SPD-processed titanium [86].

It is important to note about a possible source of error related to the single K and α values determined for the different equivalent strain regimes. Since microstructural refinement and dislocation substructure formation depends on the imparted equivalent strain, the K and α values should also evolve with the number of HPT-rotations. α is related to the arrangement of dilocations which can be either homogeneous or forming subgrains depending on the (α+β) colony orientations (**Section 3.2**). Similarly, the substructure evolution is represented by well-defined nano-crystalline α-grains after 10 HPT rotations which should produce a different α-value (**Section 3.3**). Accordingly, it follows that the use of single values of K and α probably contribute to the under and/or overestimations of the mesured strength for different HPT-processed alloys. The strength modeling suggests, however, that the dislocation density is more dominant than microstrucural refinement so that a single α value is more errorneous than a single K value for the different equivalent strain regimes.

5. Summary and conclusions

In this investigation HPT processing was carried out for unmodified and boron-modified Ti-6Al-4V alloys in the as-cast and β-forged conditions for varying numbers of rotations. After HPT processing, the alloys were studied for microstructure and substructure evolution and the ensuing effect on the mechanical response. The major conclusions are as follows:

- A starting microstructural difference between the as-cast alloys significantly influences the microstructure evolution at lower equivalent strains. While the unmodified alloy represents homogeneous microstructure with pronounced dislocation substructure, the boron-modified alloy is characterized by deformation inhomogeneity and micro-bands. In the β-forged condition, both alloys exhibit inhomogeneous deformation and micro-band formation in HPT processing due to their similar starting microstrutures while TiB particles contribute further to the deformation heterogeneities for the boron-modified alloy.
- While certain of the (α+β)-colony orientations lead to sub-grain formation and macroscopic shear banding, other orientations deform by micro-banding without substructure formation for the as-cast unmodified alloy. The as-cast or β-forged boron-modified alloys as well as the unmodified β-forged alloy exhibit micro-banding without substructure formation irrespective of the (α+β)-colony oorientation. The refined microstructure and low aspect

ratio of α-lamellae as well as TiB particles for the boron-modified alloys produce dislocation pile ups which mitigate the orientation differences of slip activation.

- Microstructure evolution after extreme straining, up to 10 HPT rotations, is characterized by well-devolved nanocrystalline, defect free equiaxed grains plus elongated α-grains for all alloys. The TiB particles do not influence the deformation response in the large strain regime.
- The as-cast unmodified alloy produces rapid fragmentation of α-lamellae only during the intermediate and extreme strain regimes. The other alloys continue with α-lamellae fragmentation from the beginning with increasing strain due to the refined starting microstructures.
- By considering a linear summation between Hall-Petch and Taylor strengthening, an evaluation of strength modeling suggests that both the microstructural refinement and dislocation substructure evolution influences the mechanical response and hardness variation of the alloys from the initial stages of HPT processing up to 10 rotations.

Acknowledgements

Two of the authors (TGL and YH) were supported by the European Research Council under ERC Grant Agreement No. 267464-SPDMETALS. SS & SR acknowledge Dr. Dan Miracle of AFRL and Dr. S. Tamirisakandala of FMW Composites for the alloy used and the Indian Institute of Science, Bangalore, India, for provision of the necessary research facilities.

References

[1] D. Banerjee, J.C. Williams, Perspectives on Titanium Science and Technology, Acta Materialia 61(3) (2013) 844-879.
[2] J.P. Davim, Machining of Titanium Alloys, Springer Berlin 2014.
[3] P.A. Kobryn, S.L. Semiatin, Microstructure and texture evolution during solidification processing of Ti-6Al-4V, Journal of Materials Processing Technology 135(2-3) (2003) 330-339.
[4] S. Roy, S. Suwas, S. Tamirisakandala, D.B. Miracle, R. Srinivasan, Development of solidification microstructure in boron-modified alloy Ti–6Al–4V–0.1B, Acta Materialia 59(14) (2011) 5494-5510.
[5] S. Tamirisakandala, R.B. Bhat, J.S. Tiley, D.B. Miracle, Grain refinement of cast titanium alloys via trace boron addition, Scripta Materialia 53(12) (2005) 1421-1426.
[6] I. Sen, S. Tamirisakandala, D.B. Miracle, U. Ramamurty, Microstructural effects on the mechanical behavior of B-modified Ti-6Al-4V alloys, Acta Materialia 55(15) (2007) 4983-4993.
[7] I. Sen, K. Gopinath, R. Datta, U. Ramamurty, Fatigue in Ti-6Al-4V-B alloys, Acta Materialia 58(20) (2010) 6799-6809.
[8] S. Tamirisakandala, R.B. Bhat, J.S. Tiley, D.B. Miracle, Processing, microstructure, and properties of Î² titanium alloys modified with boron, Journal of Materials Engineering and Performance 14(6) (2005) 741-746.
[9] S. Roy, S. Suwas, S. Tamirisakandala, R. Srinivasan, D.B. Miracle, Microstructure and texture evolution during β extrusion of boron modified Ti-6Al-4V alloy, Materials Science and Engineering A 540 (2012) 152-163.

[10] S. Roy, S. Suwas, Microstructure and Texture Evolution During Sub-Transus Thermomechanical Processing of Ti-6Al-4V-0.1B Alloy: Part I. Hot Rolling in (α + β) Phase Field, Metall and Mat Trans A (2013) 1-19.
[11] S. Roy, S. Karanth, S. Suwas, Microstructure and Texture Evolution During Sub-Transus Thermo-Mechanical Processing of Ti-6Al-4V-0.1B Alloy: Part II. Static Annealing in (α + β) Regime, Metall and Mat Trans A (2013) 1-15.
[12] S. Roy, S. Suwas, The influence of temperature and strain rate on the deformation response and microstructural evolution during hot compression of a titanium alloy Ti–6Al–4V–0.1B, Journal of Alloys and Compounds 548 (2013) 110-125.
[13] S. Roy, R. Madhavan, S. Suwas, Crystallographic texture and microstructure evolution during hot compression of Ti-6Al-4V-0.1B alloy in the (α + β)-regime, Philosophical Magazine 94(4) (2013) 358-380.
[14] S. Roy, A. Sarkar, S. Suwas, On characterization of deformation microstructure in Boron modified Ti-6Al-4V alloy, Materials Science and Engineering: A 528(1) (2010) 449-458.
[15] S. Roy, S. Suwas, On the absence of shear cracking and grain boundary cavitation in secondary tensile regions of Ti-6Al-4V-0.1B alloy during hot (α + β)-compression, Philosophical Magazine 94(5) (2013) 447-463.
[16] S. Roy, S. Suwas, Deformation mechanisms during superplastic testing of Ti–6Al–4V–0.1B alloy, Materials Science and Engineering: A 574 (2013) 205-217.
[17] S. Roy, S. Suwas, Enhanced superplasticity for (α + β)-hot rolled Ti–6Al–4V–0.1B alloy by means of dynamic globularization, Materials & Design 58 (2014) 52-64.
[18] V. Sinha, R. Srinivasan, S. Tamirisakandala, D.B. Miracle, Superplastic behavior of Ti–6Al–4V–0.1B alloy, Materials Science and Engineering: A 539(0) (2012) 7-12.
[19] R.Z. Valiev, R.K. Islamgaliev, I.V. Alexandrov, Bulk nanostructured materials from severe plastic deformation, Progress in Materials Science 45(2) (2000) 103-189.
[20] R.Z. Valiev, B. Straumal, T.G. Langdon, Using Severe Plastic Deformation to Produce Nanostructured Materials with Superior Properties, Annual Review of Materials Research 52(1) (2022) 357-382.
[21] K. Edalati, A. Bachmaier, V.A. Beloshenko, Y. Beygelzimer, V.D. Blank, W.J. Botta, K. Bryła, J. Čížek, S. Divinski, N.A. Enikeev, Y. Estrin, G. Faraji, R.B. Figueiredo, M. Fuji, T. Furuta, T. Grosdidier, J. Gubicza, A. Hohenwarter, Z. Horita, J. Huot, Y. Ikoma, M. Janeček, M. Kawasaki, P. Král, S. Kuramoto, T.G. Langdon, D.R. Leiva, V.I. Levitas, A. Mazilkin, M. Mito, H. Miyamoto, T. Nishizaki, R. Pippan, V.V. Popov, E.N. Popova, G. Purcek, O. Renk, Á. Révész, X. Sauvage, V. Sklenicka, W. Skrotzki, B.B. Straumal, S. Suwas, L.S. Toth, N. Tsuji, R.Z. Valiev, G. Wilde, M.J. Zehetbauer, X. Zhu, Nanomaterials by severe plastic deformation: review of historical developments and recent advances, Materials Research Letters 10(4) (2022) 163-256.
[22] H. Azzeddine, D. Bradai, T. Baudin, T.G. Langdon, Texture evolution in high-pressure torsion processing, Progress in Materials Science 125 (2022) 100886.
[23] Z. Zhang, Z. Qu, L. Xu, R. Liu, P. Zhang, Z. Zhang, T.G. Langdon, Relationship between strength and uniform elongation of metals based on an exponential hardening law, Acta Materialia 231 (2022) 117866.
[24] R.B. Figueiredo, T.G. Langdon, Effect of grain size on strength and strain rate sensitivity in metals, Journal of Materials Science 57(8) (2022) 5210-5229.
[25] I.J. Beyerlein, J.R. Mayeur, S. Zheng, N.A. Mara, J. Wang, A. Misra, Emergence of stable interfaces under extreme plastic deformation, Proceedings of the National Academy of Sciences of the United States of America 111(12) (2014) 4386-4390.
[26] A. Azushima, R. Kopp, A. Korhonen, D.Y. Yang, F. Micari, G.D. Lahoti, P. Groche, J. Yanagimoto, N. Tsuji, A. Rosochowski, A. Yanagida, Severe plastic deformation (SPD) processes for metals, CIRP Annals 57(2) (2008) 716-735.
[27] Y. Huang, T.G. Langdon, Advances in ultrafine-grained materials, Materials Today 16(3) (2013) 85-93.

[28] Y. Estrin, A. Vinogradov, Extreme grain refinement by severe plastic deformation: A wealth of challenging science, Acta Materialia 61(3) (2013) 782-817.
[29] T.G. Langdon, Twenty-five years of ultrafine-grained materials: Achieving exceptional properties through grain refinement, Acta Materialia 61(19) (2013) 7035-7059.
[30] R.Z. Valiev, A.P. Zhilyaev, T.G. Langdon, Principles and Technical Parameters of High-Pressure Torsion, Bulk Nanostructured Materials: Fundamentals and Applications, Wiley/TMS, Hoboken, NJ 2014.
[31] A.P. Zhilyaev, T.G. Langdon, Using high-pressure torsion for metal processing: Fundamentals and applications, Progress in Materials Science 53(6) (2008) 893-979.
[32] K. Edalati, Z. Horita, A review on high-pressure torsion (HPT) from 1935 to 1988, Materials Science and Engineering: A 652 (2016) 325-352.
[33] A. Hohenwarter, Incremental high pressure torsion as a novel severe plastic deformation process: Processing features and application to copper, Materials Science and Engineering: A 626 (2015) 80-85.
[34] W. Chen, J. Xu, C. Ding, D. Shan, B. Guo, T.G. Langdon, Fracture mechanism of electrically-assisted micro-tension in nanostructured titanium using synchrotron radiation X-ray tomography, Scripta Materialia 222 (2023) 114997.
[35] H.-K. Lin, Y.-H. Cheng, G.-Y. Li, Y.-C. Chen, P. Bazarnik, J. Muzy, Y. Huang, T.G. Langdon, Study on the Surface Modification of Nanostructured Ti Alloys and Coarse-Grained Ti Alloys, Metals 12(6) (2022) 948.
[36] K. Sun, B. Sun, X. Yi, Y. Yaqian, X. Meng, Z. Gao, W. Cai, The microstructure and martensitic transformation of Ti-13 V-3Al light weight shape memory alloy deformed by high-pressure torsion, Journal of Alloys and Compounds 895 (2022) 162612.
[37] S.H.M. Anijdan, H.R. Koohdar, M. Nili-Ahmadabadi, H.R. Jafarian, T.G. Langdon, Evaluation of texture weakening and microstructural evolution in an Fe–10Ni–7Mn martensitic steel severely deformed by six turns of high-pressure torsion, Materials Science and Engineering: A 851 (2022) 143660.
[38] X. Ren, X. An, S. Ni, Y. Huang, M. Song, Formation of nanocrystalline grain structure in an Mg-Gd-Y-Zr alloy processed by high-pressure torsion, Materials Characterization 191 (2022) 112088.
[39] I. Sen, U. Ramamurty, Elastic modulus of Ti-6Al-4V-xB alloys with B up to 0.55 wt.%, Scripta Materialia 62(1) (2010) 37-40.
[40] A. Bommakanti, S. Roy, S. Suwas, Effect of hypoeutectic boron modification on the dynamic properties of Ti-6Al-4V alloy, Journal of Materials Research 31(18) (2016) 2804-2816.
[41] S. Roy, V. Tungala, S. Suwas, Effect of hypoeutectic boron addition on the β transus of Ti-6Al-4V alloy, Metallurgical and Materials Transactions A: Physical Metallurgy and Materials Science 42(9) (2011) 2535-2541.
[42] Y.C. Wang, T.G. Langdon, Effect of heat treatment on microstructure and microhardness evolution in a Ti–6Al–4V alloy processed by high-pressure torsion, Journal of Materials Science 48(13) (2013) 4646-4652.
[43] S. Roy, S. Suwas, Orientation dependent spheroidization response and macro-zone formation during sub β-transus processing of Ti-6Al-4V alloy, Acta Materialia 134 (2017) 283-301.
[44] D. Chen, J.-C. Kuo, W.-T. Wu, Effect of microscopic parameters on EBSD spatial resolution, Ultramicroscopy 111(9) (2011) 1488-1494.
[45] A. Sarkar, S. Roy, S. Suwas, X-ray diffraction line profile analysis of deformation microstructure in boron modified Ti–6Al–4V alloy, Materials Characterization 62(1) (2011) 35-42.
[46] G. Ribárik, T. Ungár, J. Gubicza, MWP-fit: a program for multiple whole-profile fitting of diffraction peak profiles by ab initio theoretical functions, Journal of Applied Crystallography 34(5) (2001) 669-676.
[47] B.D. Cullity, Elements of X-ray Diffraction, Addison-Wesley, Reading, MA, USA 1978.
[48] G. Williamson, W. Hall, X-ray line broadening from filed aluminium and wolfram, Acta Metallurgica 1(1) (1953) 22-31.

[49] D. Balzar, H. Ledbetter, Voigt-function modeling in Fourier analysis of size- and strain-broadened X-ray diffraction peaks, Journal of Applied Crystallography 26(1) (1993) 97-103.
[50] A.R. Stokes, A Numerical Fourier-analysis Method for the Correction of Widths and Shapes of Lines on X-ray Powder Photographs, Proceedings of the Physical Society 61(4) (1948) 382.
[51] T. Ungár, A. Borbély, The effect of dislocation contrast on x-ray line broadening: A new approach to line profile analysis, Applied Physics Letters 69(21) (1996) 3173-3175.
[52] G. Ribarik, T. Ungar, J. Gubicza, MWP-fit: a program for multiple whole-profile fitting of diffraction peak profiles by ab initio theoretical functions, Journal of Applied Crystallography 34(5) (2001) 669-676.
[53] M. Wilkens, The determination of density and distribution of dislocations in deformed single crystals from broadened X-ray diffraction profiles, Physica status solidi (a) 2(2) (1970) 359-370.
[54] G. Ribárik, J. Gubicza, T. Ungár, Correlation between strength and microstructure of ball-milled Al–Mg alloys determined by X-ray diffraction, Materials science and engineering: A 387 (2004) 343-347.
[55] S. Roy, S.S. D, S. Suwas, S. Kumar, K. Chattopadhyay, Microstructure and texture evolution during accumulative roll bonding of aluminium alloy AA5086, Materials Science and Engineering: A 528(29) (2011) 8469-8478.
[56] J. Lins, H. Sandim, K. Vecchio, D. Raabe, An EBSD Investigation on Deformation-Induced Shear Bands in Ti-Bearing IF-Steel under Controlled Shock-Loading Conditions, Materials Science Forum 495-497 (2005) 393-398.
[57] M.A. Meyers, Y.B. Xu, Q. Xue, M.T. Pérez-Prado, T.R. McNelley, Microstructural evolution in adiabatic shear localization in stainless steel, Acta Materialia 51(5) (2003) 1307-1325.
[58] F.J. Humphreys, M. Hatherly, Chapter 2 - The Deformed State, in: F.J. Humphreys, M. Hatherly (Eds.), Recrystallization and Related Annealing Phenomena (Second Edition), Elsevier, Oxford, 2004, pp. 11-II.
[59] J. Gil Sevillano, E. Aernoudt, Low energy dislocation structures in highly deformed materials, Materials Science and Engineering 86 (1987) 35-51.
[60] D. Kuhlmann-Wilsdorf, Theory of plastic deformation: - properties of low energy dislocation structures, Materials Science and Engineering: A 113 (1989) 1-41.
[61] A.V. Podolskiy, C. Mangler, E. Schafler, E.D. Tabachnikova, M.J. Zehetbauer, Microstructure and mechanical properties of high purity nanostructured titanium processed by high pressure torsion at temperatures 300 and 77 K, Journal of Materials Science 48(13) (2013) 4689-4697.
[62] H. Shahmir, T.G. Langdon, Using heat treatments, high-pressure torsion and post-deformation annealing to optimize the properties of Ti-6Al-4V alloys, Acta Materialia 141 (2017) 419-426.
[63] H. Shahmir, T.G. Langdon, An evaluation of the hexagonal close-packed to face-centered cubic phase transformation in a Ti-6Al-4V alloy during high-pressure torsion, Materials Science and Engineering: A 704 (2017) 212-217.
[64] T. Ungár, I. Alexandrov, M. Zehetbauer, Ultrafine-grained microstructures evolving during severe plastic deformation, JOM 52(4) (2000) 34-36.
[65] R.Z. Valiev, I.P. Semenova, V.V. Latysh, H. Rack, T.C. Lowe, J. Petruzelka, L. Dluhos, D. Hrusak, J. Sochova, Nanostructured Titanium for Biomedical Applications, Advanced Engineering Materials 10(8) (2008) B15-B17.
[66] A. Dehghan-Manshadi, R.J. Dippenaar, Strain-induced phase transformation during thermo-mechanical processing of titanium alloys, Materials Science and Engineering: A 552 (2012) 451-456.
[67] J. Wang, Z. Horita, M. Furukawa, M. Nemoto, N.K. Tsenev, R.Z. Valiev, Y. Ma, T.G. Langdon, An investigation of ductility and microstructural evolution in an Al−3% Mg alloy with submicron grain size, Journal of Materials Research 8(11) (1993) 2810-2818.
[68] Z. Horita, D.J. Smith, M. Furukawa, M. Nemoto, R.Z. Valiev, T.G. Langdon, An investigation of grain boundaries in submicrometer-grained Al-Mg solid solution alloys using high-resolution electron microscopy, Journal of Materials Research 11(8) (1996) 1880-1890.

[69] Z.-Y. Hu, X.-W. Cheng, Z.-H. Zhang, H. Wang, S.-L. Li, G.F. Korznikova, D.V. Gunderov, F.-C. Wang, The influence of defect structures on the mechanical properties of Ti-6Al-4V alloys deformed by high-pressure torsion at ambient temperature, Materials Science and Engineering: A 684 (2017) 1-13.
[70] A. Sarkar, A. Bhowmik, S. Suwas, Microstructural characterization of ultrafine-grain interstitial-free steel by X-ray diffraction line profile analysis, Applied Physics A 94(4) (2009) 943-948.
[71] H. Jiang, Y.T. Zhu, D.P. Butt, I.V. Alexandrov, T.C. Lowe, Microstructural evolution, microhardness and thermal stability of HPT-processed Cu, Materials Science and Engineering: A 290(1) (2000) 128-138.
[72] H.-J. Lee, S.K. Lee, K.H. Jung, G.A. Lee, B. Ahn, M. Kawasaki, T.G. Langdon, Evolution in hardness and texture of a ZK60A magnesium alloy processed by high-pressure torsion, Materials Science and Engineering: A 630 (2015) 90-98.
[73] C.T. Wang, A.G. Fox, T.G. Langdon, Microstructural evolution in ultrafine-grained titanium processed by high-pressure torsion under different pressures, Journal of Materials Science 49(19) (2014) 6558-6564.
[74] F. Cao, E.K. Cerreta, C.P. Trujillo, G.T. Gray, Dynamic tensile extrusion response of tantalum, Acta Materialia 56(19) (2008) 5804-5817.
[75] S. Mahesh, Deformation banding and shear banding in single crystals, Acta Materialia 54(17) (2006) 4565-4574.
[76] X. Huang, N. Hansen, Grain orientation dependence of microstructure in aluminium deformed in tension, Scripta Materialia 37(1) (1997) 1-7.
[77] Y. Kawasaki, T. Takeuchi, Cell structures in copper single crystals deformed in the [001] and [111] axes, Scripta Metallurgica 14(2) (1980) 183-188.
[78] K. Morii, H. Mecking, Y. Nakayama, Development of shear bands in f.c.c. single crystals, Acta Metallurgica 33(3) (1985) 379-386.
[79] S. Roy, S. Suwas, Unique texture transition during sub β-transus annealing of warm-rolled Ti-6Al-4V alloy: Role of orientation dependent spheroidization, Scripta Materialia 154 (2018) 1-7.
[80] W.F. Hosford., The mechanics of crystals and textured polycrystals, Oxford University Press, New York-Oxford 1994.
[81] S.L. Semiatin, T.R. Bieler, The effect of alpha platelet thickness on plastic flow during hot working of Ti-6Al-4V with a transformed microstructure, Acta Materialia 49(17) (2001) 3565-3573.
[82] I.C. Dragomir, T. Ungar, Contrast factors of dislocations in the hexagonal crystal system, Journal of Applied Crystallography 35(5) (2002) 556-564.
[83] S. Roy, L.F. Allard, A. Rodriguez, W.D. Porter, A. Shyam, Comparative Evaluation of Cast Aluminum Alloys for Automotive Cylinder Heads: Part II—Mechanical and Thermal Properties, Metall and Mat Trans A 48(5) (2017) 2543-2562.
[84] H. Mughrabi, The α-factor in the Taylor flow-stress law in monotonic, cyclic and quasi-stationary deformations: Dependence on slip mode, dislocation arrangement and density, Current Opinion in Solid State and Materials Science 20(6) (2016) 411-420.
[85] A. Fattah-alhosseini, M.K. Keshavarz, Y. Mazaheri, A. Reza Ansari, M. Karimi, Strengthening mechanisms of nano-grained commercial pure titanium processed by accumulative roll bonding, Materials Science and Engineering: A 693 (2017) 164-169.
[86] Y.T. Zhu, J.Y. Huang, J. Gubicza, T. Ungár, Y.M. Wang, E. Ma, R.Z. Valiev, Nanostructures in Ti processed by severe plastic deformation, Journal of Materials Research 18(8) (2011) 1908-1917.

Figure Captions

Figure 1: SEM images (BSE mode) showing initial microstructures (before HPT processing) for (a) Ti64-C, (b) Ti64+B-C, (c) Ti64-F and (d) Ti64+B-F alloys.

Figure 2: EBSD IPF maps (superimposed with image quality) showing microstructures of (a) Ti64-C, (b) Ti64+B-C, (c) Ti64-F, and (d) Ti64+B-F alloys after one HPT rotation. Alongside

IPF maps, the change in misorientation (on a point-to-point and point-to-origin basis) within individual α-colonies is also plotted for different alloys.

Figure 3: (a), (b) TEM micrographs (brightfield mode) showing microstructure for Ti64-C alloy after 10 HPT rotations; (a) inset showing corresponding SAD pattern. Important features and observation areas are marked in these micrographs. DC, dislocation cell; LAGB, low angle grain boundary; HAGB, high angle grain boundary.

Figure 4: (a), (b) TEM micrographs (brightfield mode) showing microstructure for Ti64+B-C alloy after 10 HPT rotations. Important features and observation areas are marked in these micrographs. DC, dislocation cell; BCI, band contrast imaging.

Figure 5: (a), (b) TEM micrographs (brightfield mode) showing microstructure for Ti64-F alloy after 10 HPT rotations; (a) inset showing corresponding SAD pattern. Important features and observation areas are marked in these micrographs. DC, dislocation cell.

Figure 6: (a), (b) TEM micrographs (brightfield mode) showing microstructure for Ti64+B-F alloy after 10 HPT rotations; (a) inset showing corresponding SAD pattern. Important features and observation areas are marked in these micrographs. BCI, band contrast imaging.

Figure 7: Variation in crystallite size and micro-strain calculated from W-H analysis with HPT rotations for different alloys and conditions.

Figure 8: Variation in crystallite size and dislocation density with equivalent strain calculated from CMWP method for (a), (b) Ti64-C and Ti64+B-C alloys, respectively, and (c), (d) Ti64-F and Ti64+B-F alloys, respectively. The equivalent strain, ε, corresponding to various HPT-rotations are included in (a).

Figure 9: Hardness variation with equivalent strain for the alloys (unmodified and Boron modified) in different conditions (as-cast and β-forged).

Figure 10: σ_{measured} vs. $\sigma_{\text{calculated}}$ plots representing the contributions from various strengthening mechanisms towards strength increment in (a) Ti64-C, (b) Ti64+B-C, (c) Ti64-F and (d) Ti64+B-F alloys.

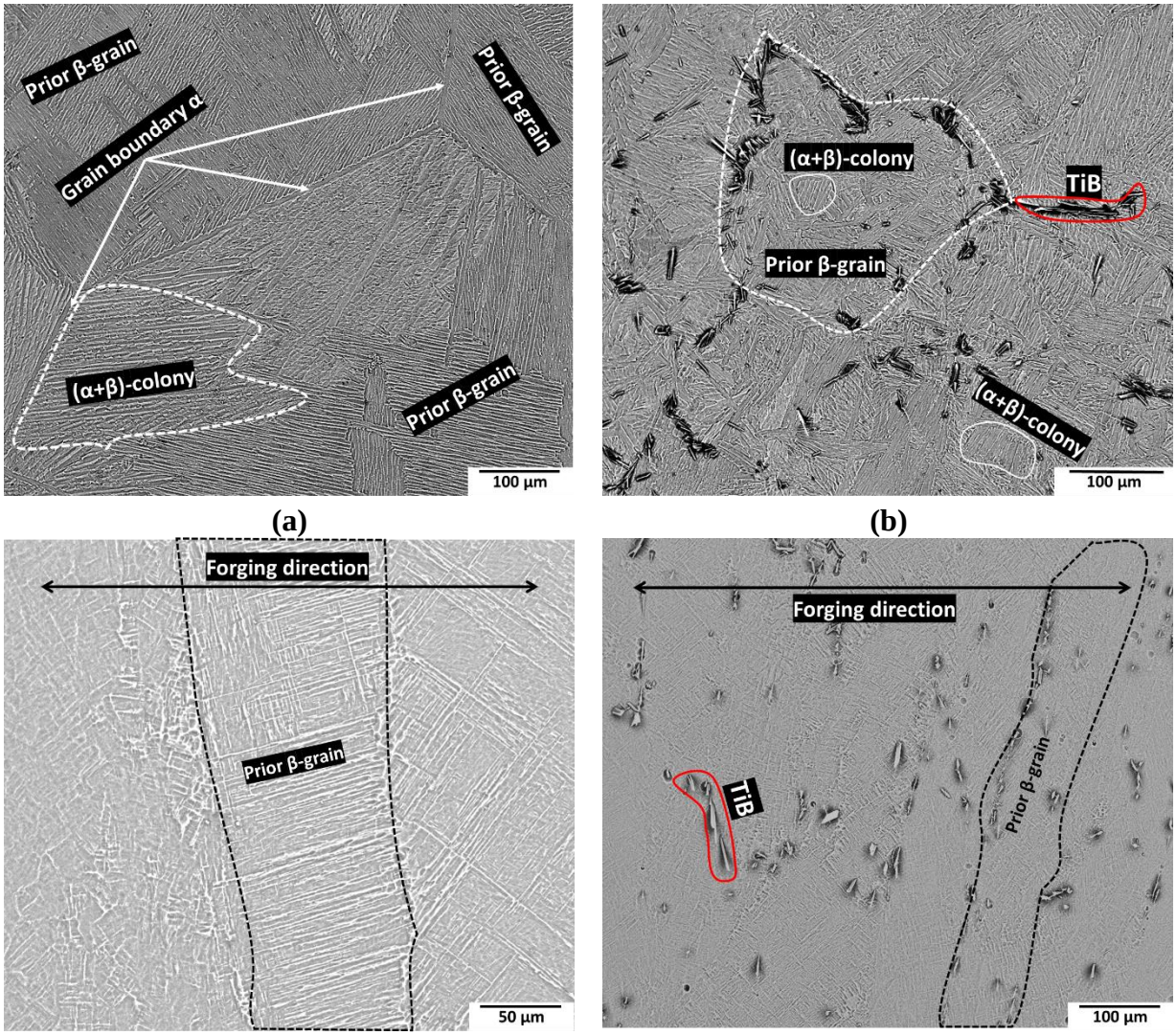

Figure 1: SEM images (BSE mode) showing initial microstructures (before HPT processing) for (a) Ti64-C, (b) Ti64+B-C, (c) Ti64-F and (d) Ti64+B-F alloys.

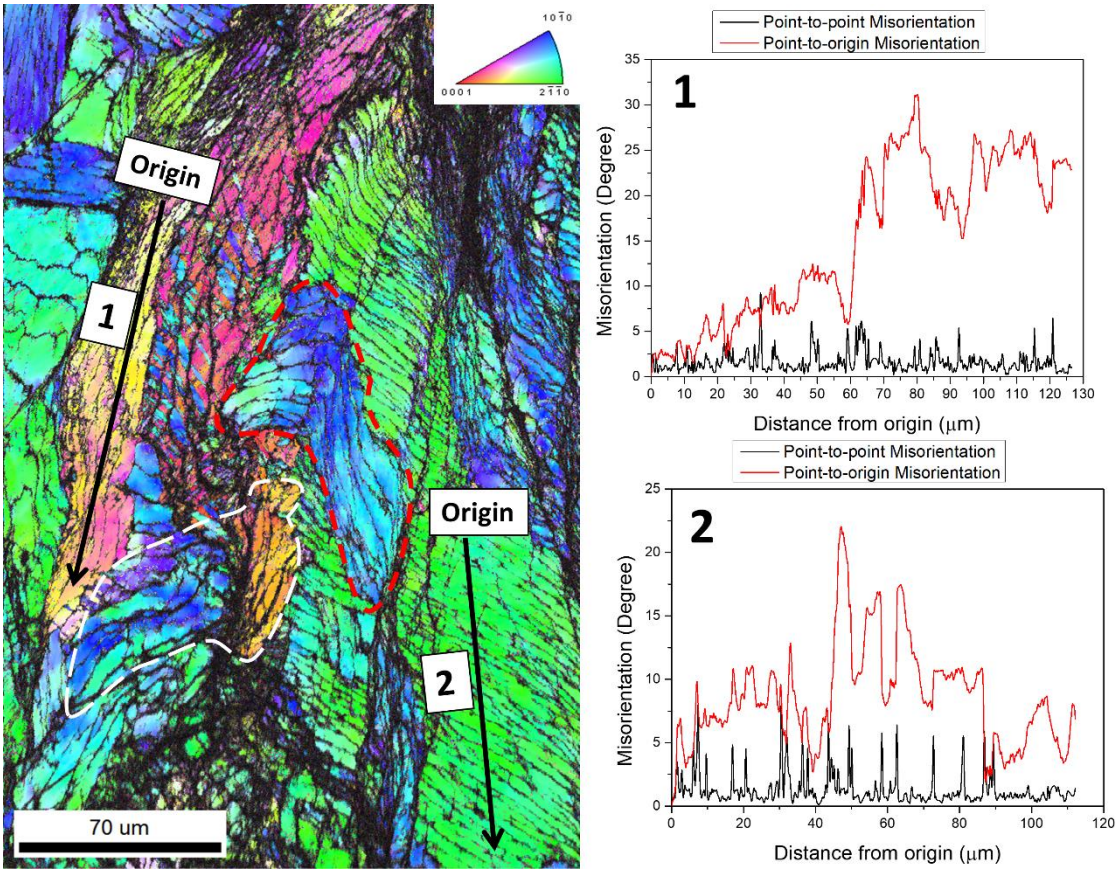
Origin
1
Origin
2
70 um
Point-to-point Misorientation
Point-to-origin Misorientation
1
Misorientation (Degree)
Distance from origin (μm)
Point-to-point Misorientation
Point-to-origin Misorientation
2
Misorientation (Degree)
Distance from origin (μm)

(a)

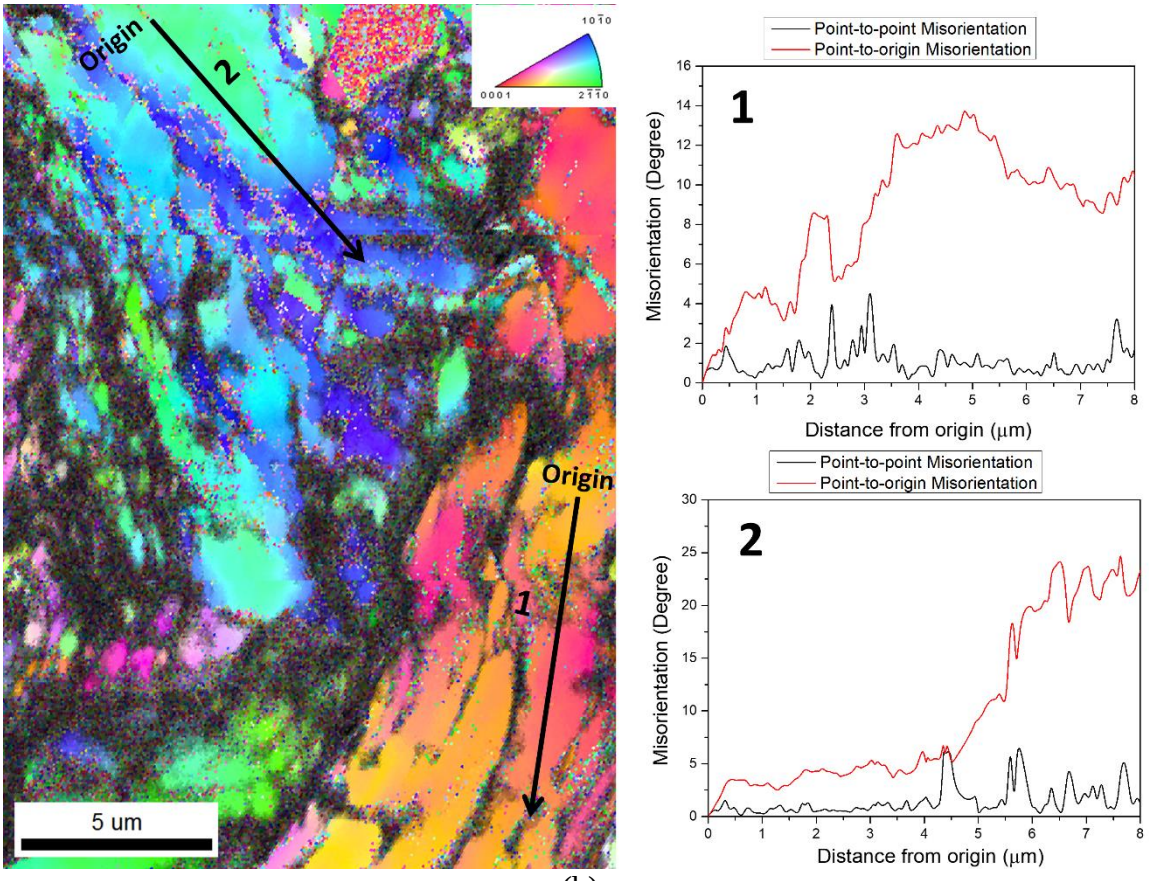
Origin
2
Origin
1
5 um
Point-to-point Misorientation
Point-to-origin Misorientation
1
Misorientation (Degree)
Distance from origin (μm)
Point-to-point Misorientation
Point-to-origin Misorientation
2
Misorientation (Degree)
Distance from origin (μm)

(b)

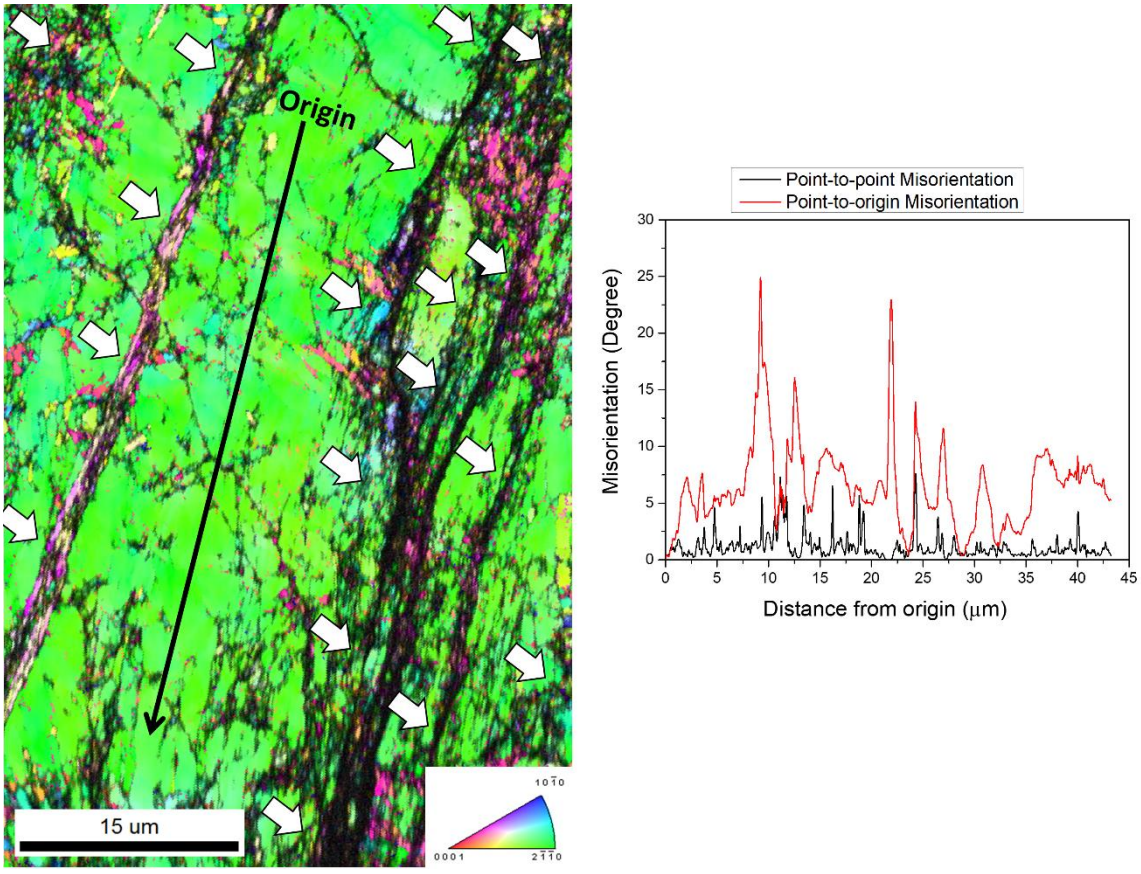

(c)

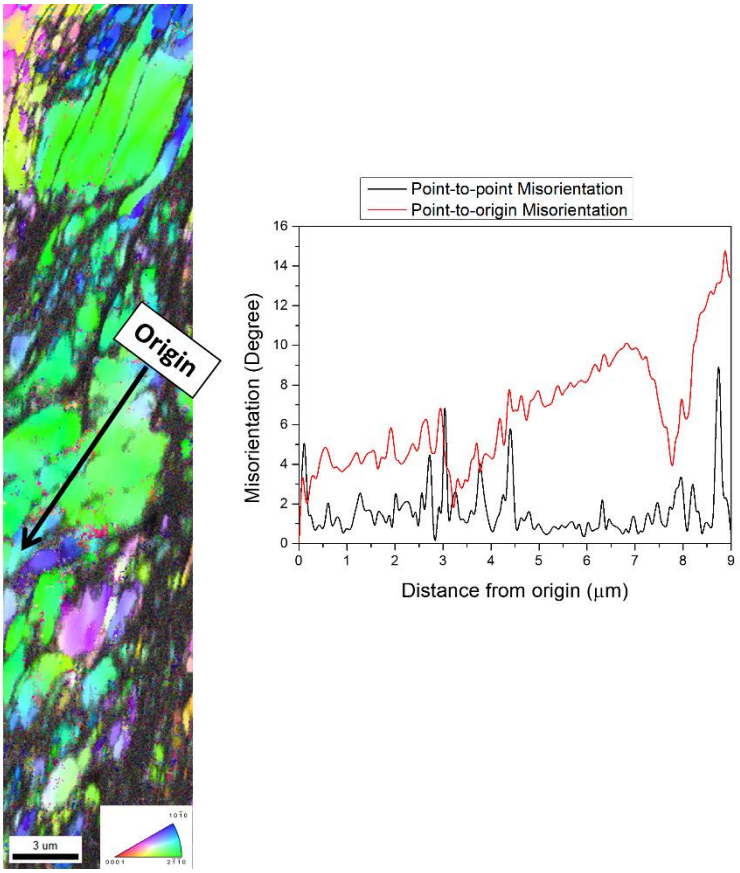

(d)

Figure 2: EBSD IPF maps (superimposed with image quality) showing microstructures of (a) Ti64-C, (b) Ti64+B-C, (c) Ti64-F, and (d) Ti64+B-F alloys after one HPT rotation. Alongside IPF maps, the change in misorientation (on a point-to-point and point-to-origin basis) within individual α-colonies is also plotted for different alloys.

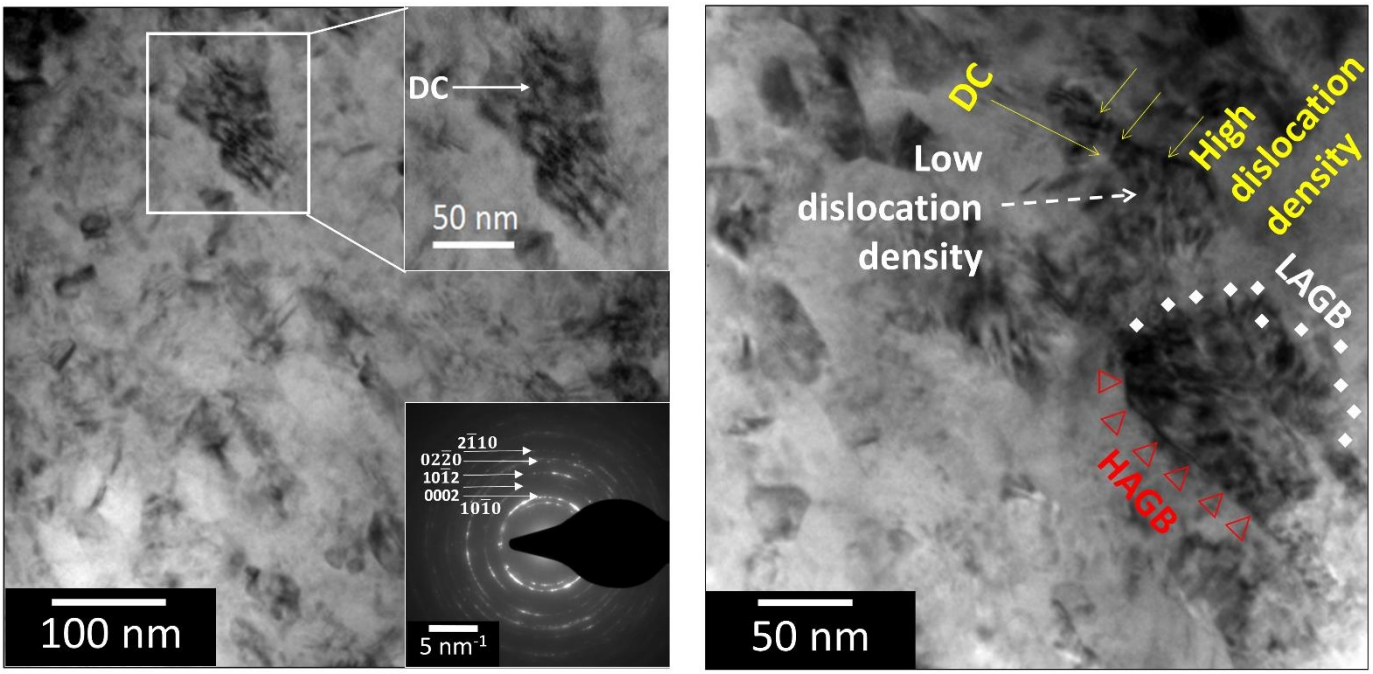

(a) (b)

Figure 3: (a), (b) TEM micrographs (brightfield mode) showing microstructure for Ti64-C alloy after 10 HPT rotations; (a) inset showing corresponding SAD pattern. Important features and observation areas are marked in these micrographs. **DC, dislocation cell; LAGB, low angle grain boundary; HAGB, high angle grain boundary.**

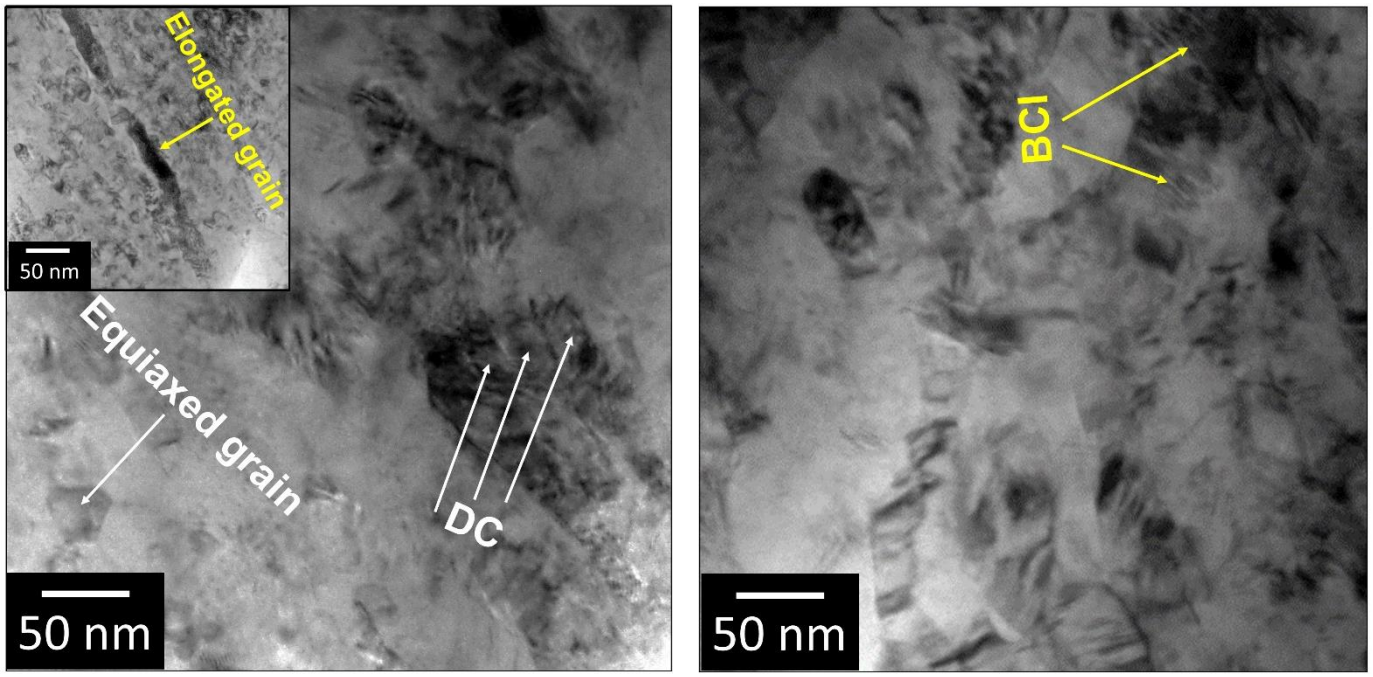

(a) (b)

Figure 4: (a), (b) TEM micrographs (brightfield mode) showing microstructure for Ti64+B-C alloy after 10 HPT rotations. Important features and observation areas are marked in these micrographs. **DC, dislocation cell; BCI, band contrast imaging.**

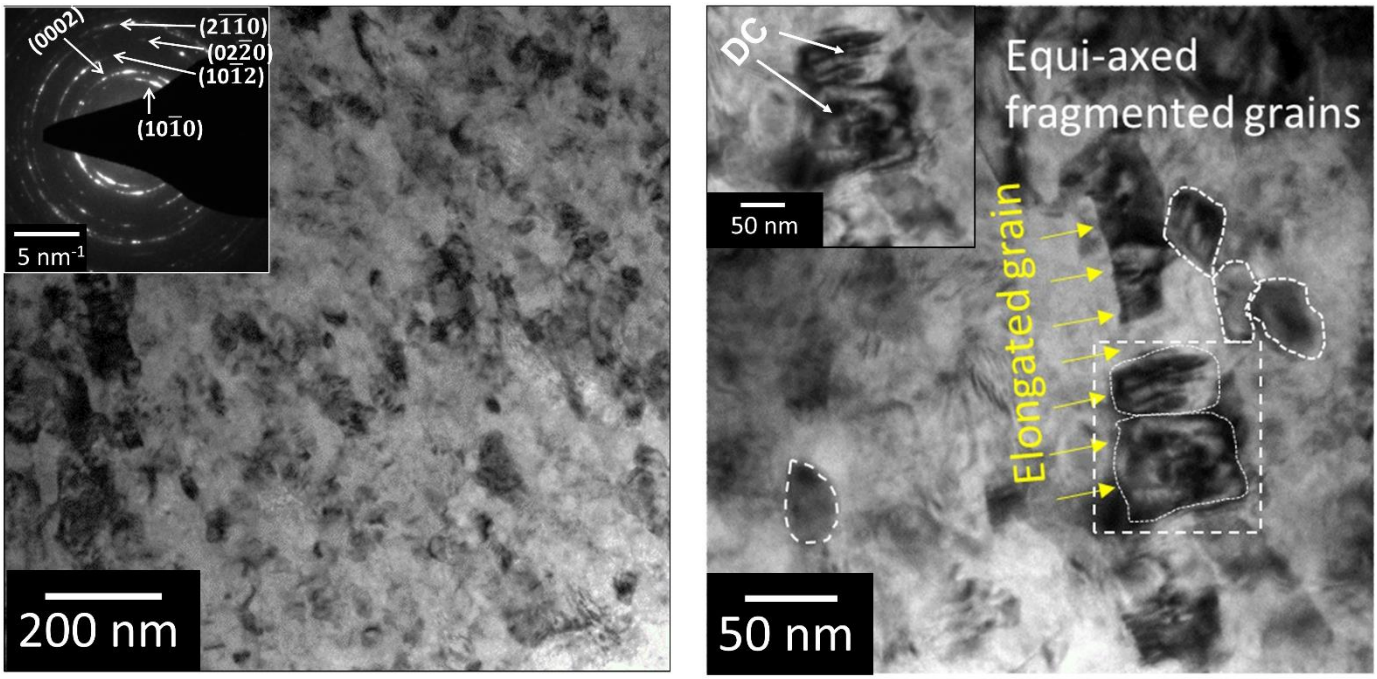

(a) (b)

Figure 5: (a), (b) TEM micrographs (brightfield mode) showing microstructure for Ti64-F alloy after 10 HPT rotations; (a) inset showing corresponding SAD pattern. Important features and observation areas are marked in these micrographs. **DC, dislocation cell.**

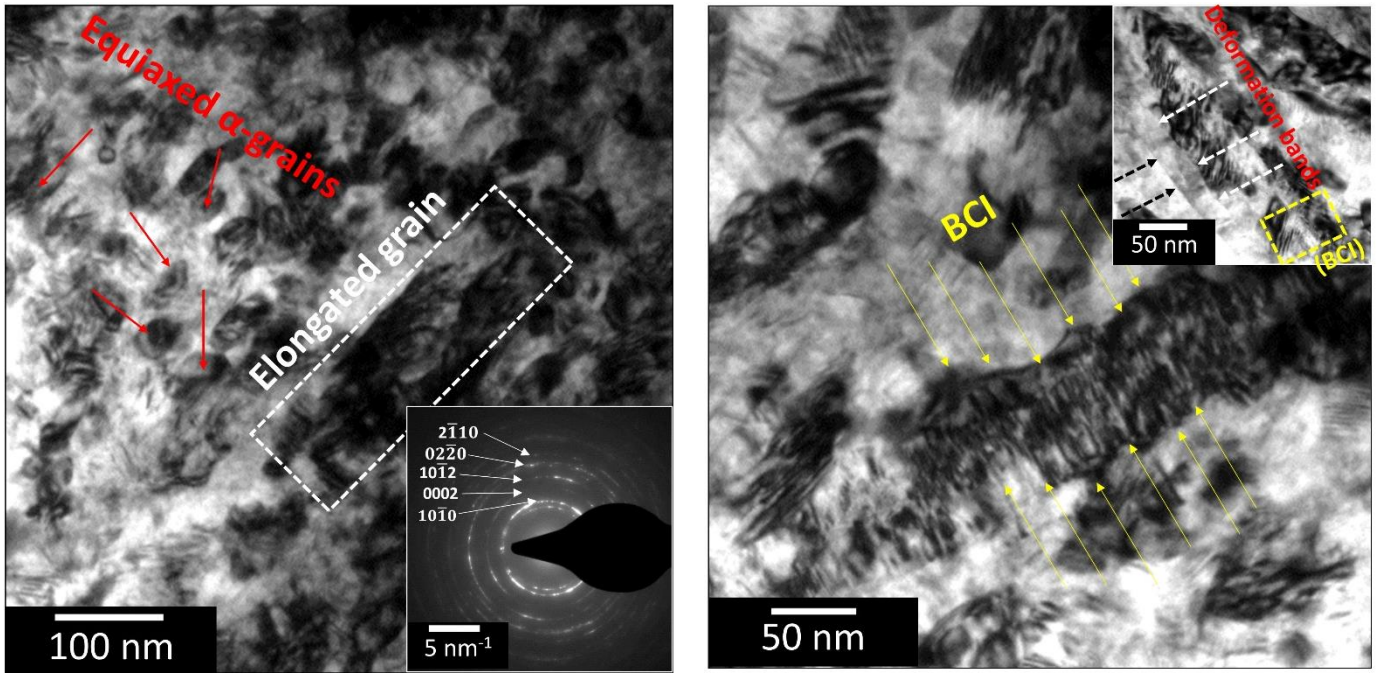

(a) (b)

Figure 6: (a), (b) TEM micrographs (brightfield mode) showing microstructure for Ti64+B-F alloy after 10 HPT rotations; (a) inset showing corresponding SAD pattern. Important features and observation areas are marked in these micrographs. **BCI, band contrast imaging.**

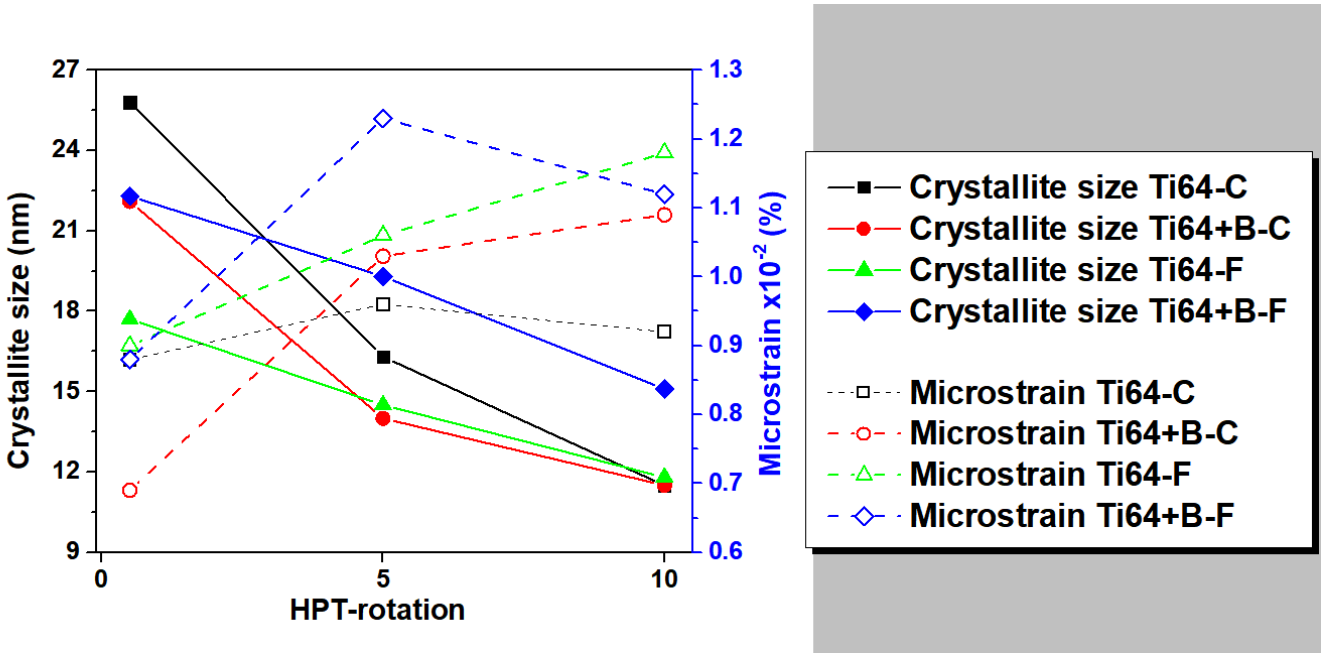

Figure 7: Variation in crystallite size and micro-strain calculated from W-H analysis with HPT rotations for different alloys and conditions.

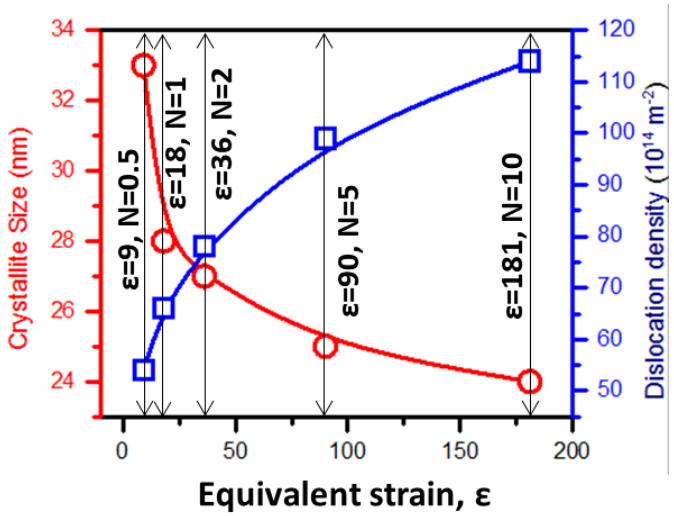

(a)

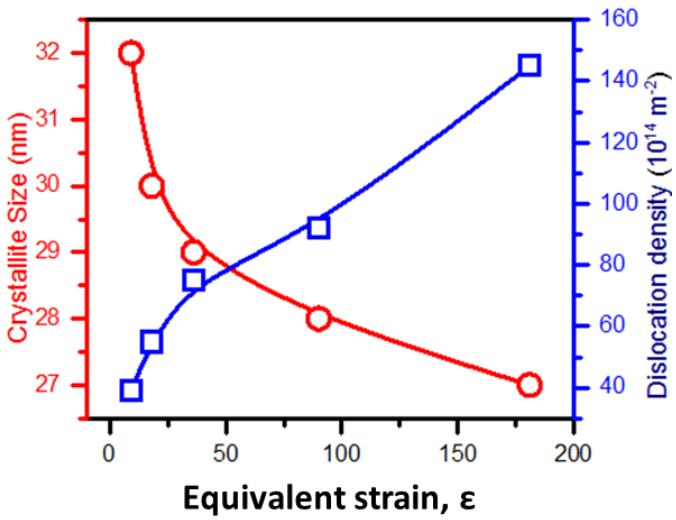

(b)

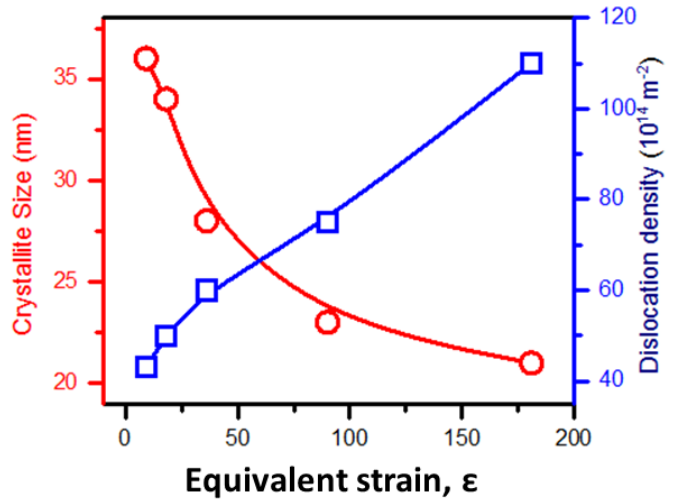

(c)

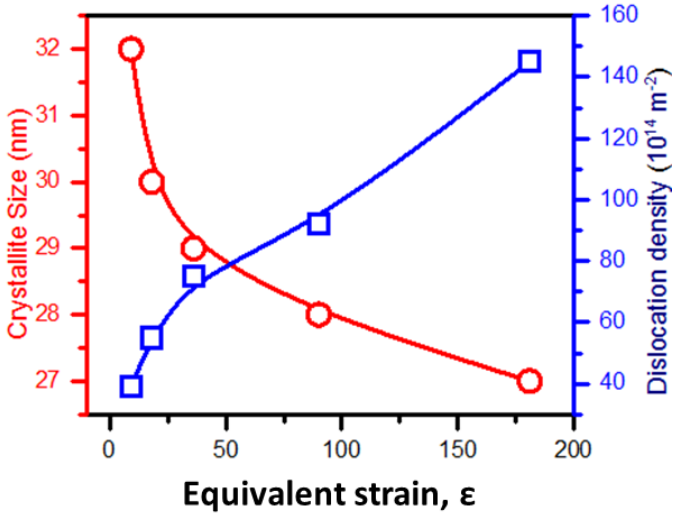

(d)

Figure 8: Variation in crystallite size and dislocation density with equivalent strain calculated from CMWP method for (a), (b) Ti64-C and Ti64+B-C alloys, respectively, and (c), (d) Ti64-F and Ti64+B-F alloys, respectively. The equivalent strain, ε, corresponding to various HPT-rotations are included in (a).

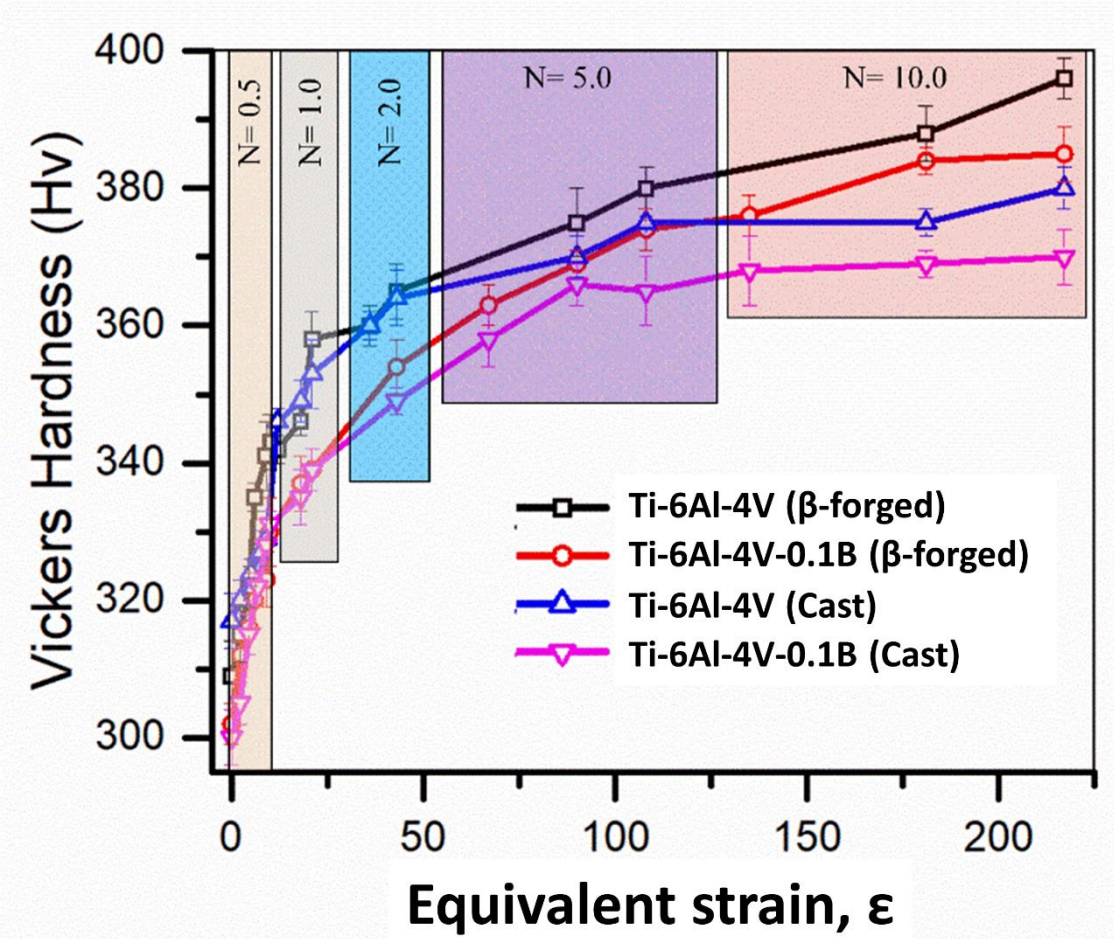

Figure 9: Hardness variation with equivalent strain for the alloys (unmodified and Boron modified) in different conditions (as-cast and β-forged).

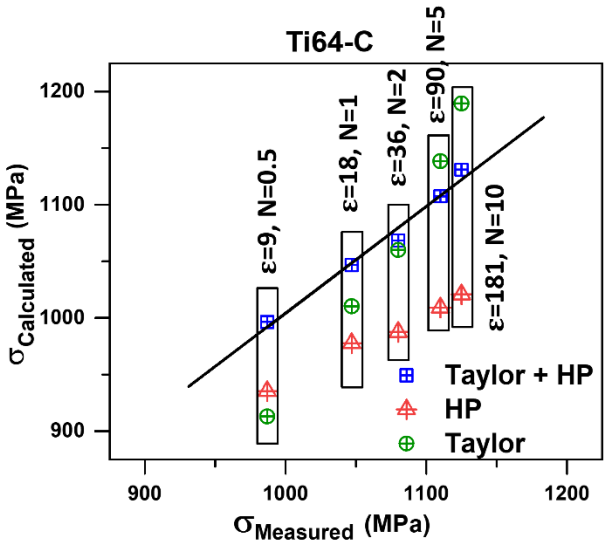

$$\sigma_{H-P+Taylor} = 440 + 0.23d^{-\frac{1}{2}} + 0.43GM\rho^{-\frac{1}{2}}$$

$$\sigma_{H-P} = 440 + 0.31d^{-\frac{1}{2}}$$

$$\sigma_{Taylor} = 440 + 1.65GM\rho^{-\frac{1}{2}}$$

(a)

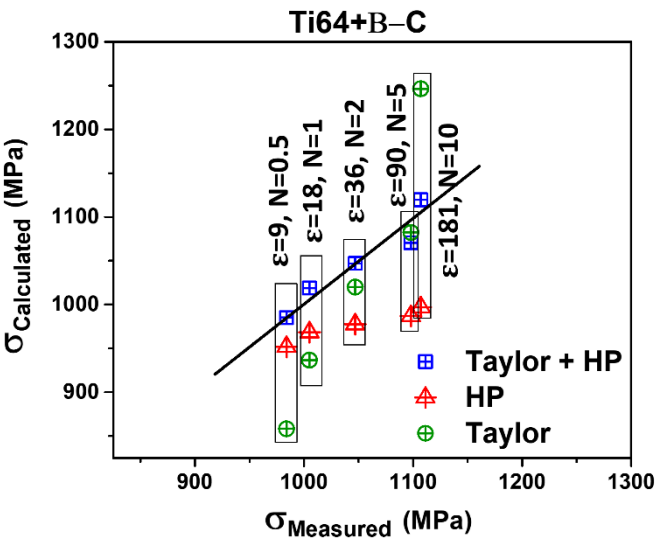

$$\sigma_{H-P+Taylor} = 440 + 2502d^{-\frac{1}{2}} + 0.43GM\rho^{-\frac{1}{2}}$$

$$\sigma_{H-P} = 440 + 2894d^{-\frac{1}{2}}$$

$$\sigma_{Taylor} = 440 + 1.78GM\rho^{-\frac{1}{2}}$$

(b)

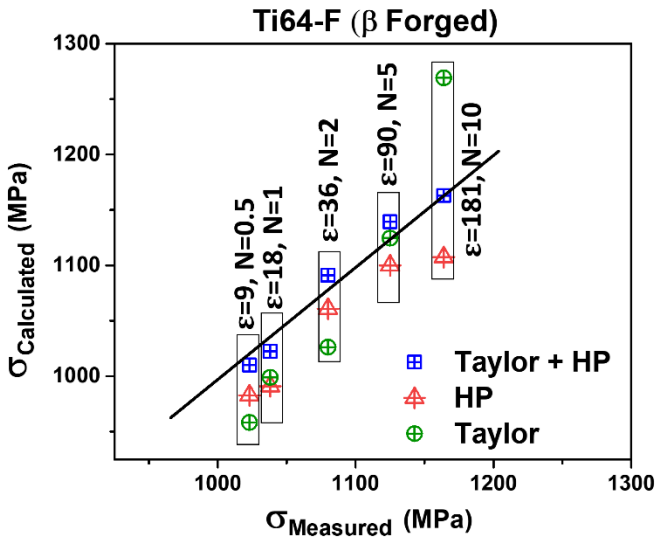

$$\sigma_{H-P+Taylor} = 440 + 2972d^{-\frac{1}{2}} + 0.27GM\rho^{-\frac{1}{2}}$$

$$\sigma_{H-P} = 440 + 3170d^{-\frac{1}{2}}$$

$$\sigma_{Taylor} = 440 + 2.03GM\rho^{-\frac{1}{2}}$$

(c)

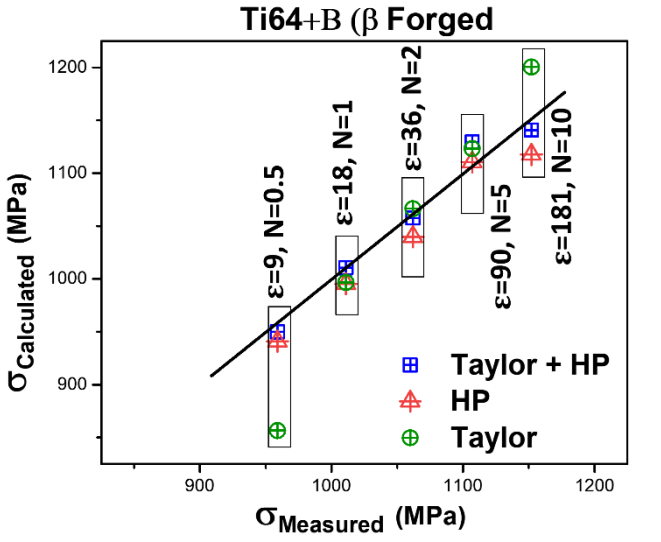

$$\sigma_{H-P+Taylor} = 440 + 3191d^{-\frac{1}{2}} + 0.1GM\rho^{-\frac{1}{2}}$$

$$\sigma_{H-P} = 440 + 3295d^{-\frac{1}{2}}$$

$$\sigma_{Taylor} = 440 + 170GM\rho^{-\frac{1}{2}}$$

(d)

Figure 10: $\sigma_{measured}$ vs. $\sigma_{calculated}$ plots representing the contributions from various strengthening mechanisms towards strength increment in (a) Ti64-C, (b) Ti64+B-C, (c) Ti64-F and (d) Ti64+B-F alloys.

Table 1. Bulk chemical composition (wt%) for Ti-6Al-4V and Ti-6Al-4V-0.1B alloys measured by inductively coupled plasma spectroscopy (ICPS) technique.

Alloy	Al	V	B	O	H	C	N	Fe	Ti
Ti64	6.6	4.1		0.18	0.008	0.02	0.01	0.23	Balance
Ti64+B	6.0	4.0	0.1	0.15	0.005	0.02	0.01	0.13	Balance

Table 2: Dislocation density (ρ), effective core cut-off radius (R_e) and dislocation arrangement parameter (M) obtained as a function of number of HPT rotations from CMWP fitting.

Alloy	Number of rotations during HPT processing	ρ x 10^{14} per m^2	R_e (nm)	M
Ti64-C	0.5	54	8.8	0.65
	5	99	4.35	0.43
	10	114	4.39	0.47
Ti64+B-C	0.5	39	11	0.70
	5	92	6.7	0.64
	10	145	5.34	0.64
Ti64-F	0.5	43	16.77	1.11
	5	75	12	1.11
	10	110	10	1.12
Ti64+B-F	0.5	42	9	0.59
	5	113	5.90	0.62
	10	140	5.19	0.63

1. Scheme of characterization for SEM-EBSD, X-ray and hardness measurement

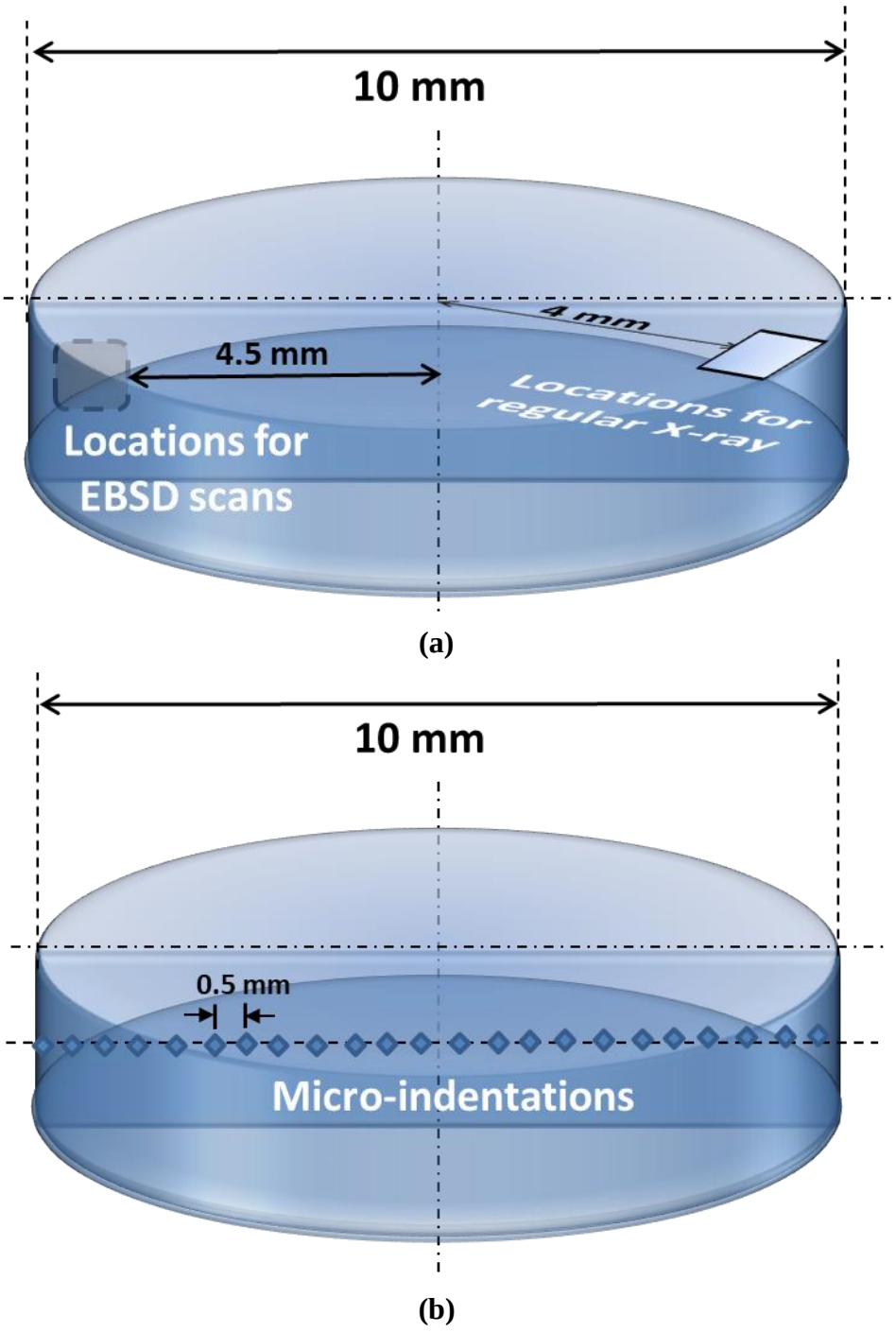

Supplementary Figure S.1: Schematic showing (a) the locations for EBSD scans and regular X-ray measurements and (b) the scheme of micro-hardness measurements on the HPT-processed discs.

2. Supplementary: TEM specimen preparation scheme.

For TEM specimen preparation, parallelepiped plates were first sectioned from the mid thickness regions of HPT-processed discs on the ND-SD plane such that the plate stretched from the center to the periphery (**Supplementary Figure S.2)**. These plates were then inserted onto the grooves in steel rods so that the periphery faced the open end (free surface) of the rods. The steel rods (along with the plates in the middle) were then fixed inside hollow steel cylinders for better grip in further preparation steps. Altogether, these assemblies (steel rods with plates in the middle and fitted inside hollow steel cylinders) had diameters of 3 mm. A specially made conducting glue was used to stick different components (specimens to the holding grips) in this assembly. Several 3 mm diameters discs were finally sliced (thickness ranging from 1-1.5 mm) from these steel rod and cylinder assemblies. These 3mm discs were thinned down electron transparency by mechanical polishing and electropolishing later in a twin-jet polisher using a solution of 10% perchloric acid and 90% ethanol.

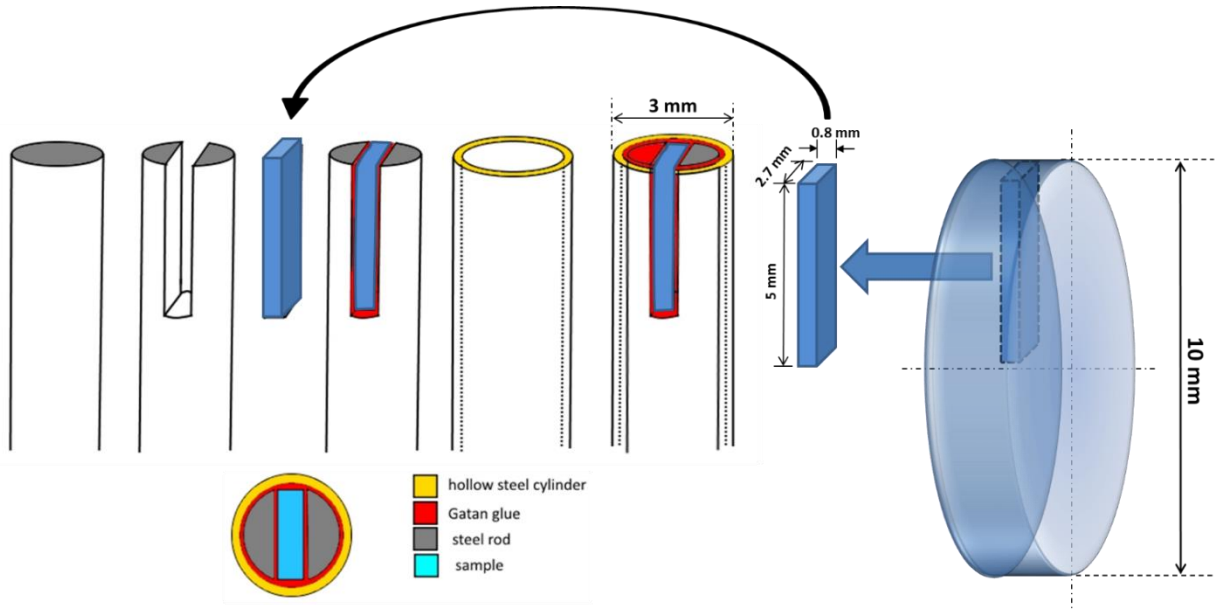

Supplementary Figure S.2: Schematic showing the preparation scheme for TEM specimens starting from HPT-processed discs.

3. Supplementary: X-ray diffraction line profile analysis (XRDLPA)

XRDLPA was carried out in the present study by two methods; conventional Williamson-Hall (WH) plotting, and convolute multiple whole profile fitting (CMWP).

3.1.Williamson-Hall (W-H) method

The classical Williamson-Hall method deconvolutes the broadening in X-ray diffraction peaks and helps to estimate the average crystallite size and micro-strain [1]. The governing equation is [2]:

$$\beta Cos(\theta)/\lambda = \left(\frac{1}{D}\right) + 2\epsilon K \text{ ..... (1)}$$

where $K = 2Sin(\theta)/\lambda$ is the diffraction vector, β is the full width at half maximum (FWHM) of corresponding XRD peak, θ is the Bragg angle, D is the crystallite size and ε is the average micro-strain. The broadening of XRD peaks usually do not represent monotonous increase with order of reflections, rather it depends on the strain anisotropy and elastic constants of α-phase [3-5]. From the dislocation based model proposed by Ungar [5], strain anisotropy contrast can be incorporated in modified Williamson-Hall analysis by replacing the parameter K with $K\sqrt{C}$, where C is the average contrast factor. The modified W-H equation is then given by:

$$(\Delta K)^2 \cong \left(\frac{0.9}{D}\right)^2 + \left(\frac{K^2 \bar{C} M^2 b^2}{2\rho}\right) + O \text{ ..... (2)}$$

where ρ and $\vec{b}$ are the average dislocation density and Burgers vector of dislocations, respectively; O stands for the higher order terms of K^2C and M is a constant that depends on outer cut-off radius of the dislocation strain field.

Supplementary Figure S.3 below display the classical Williamson-Hall plots of $\frac{2\sin\theta}{\lambda}$ *vs.* $\frac{\beta\cos\theta}{\lambda}$ for the unmodified and boron-modified alloys in the as-cast and β-forged conditions. The overall increase in full width at half maxima (FWHM) of the XRD peaks with the order of reflection for the unmodified and boron-modified alloys in the as-cast and β-forged conditions indicates a microstrain build up with increasing HPT rotations [6]. The variation in the FWHM deviates from perfect linearity for all the alloys since the classical Williamson-Hall method fails to account for the strain anisotropy in the calculation of the microstructural parameters [2].

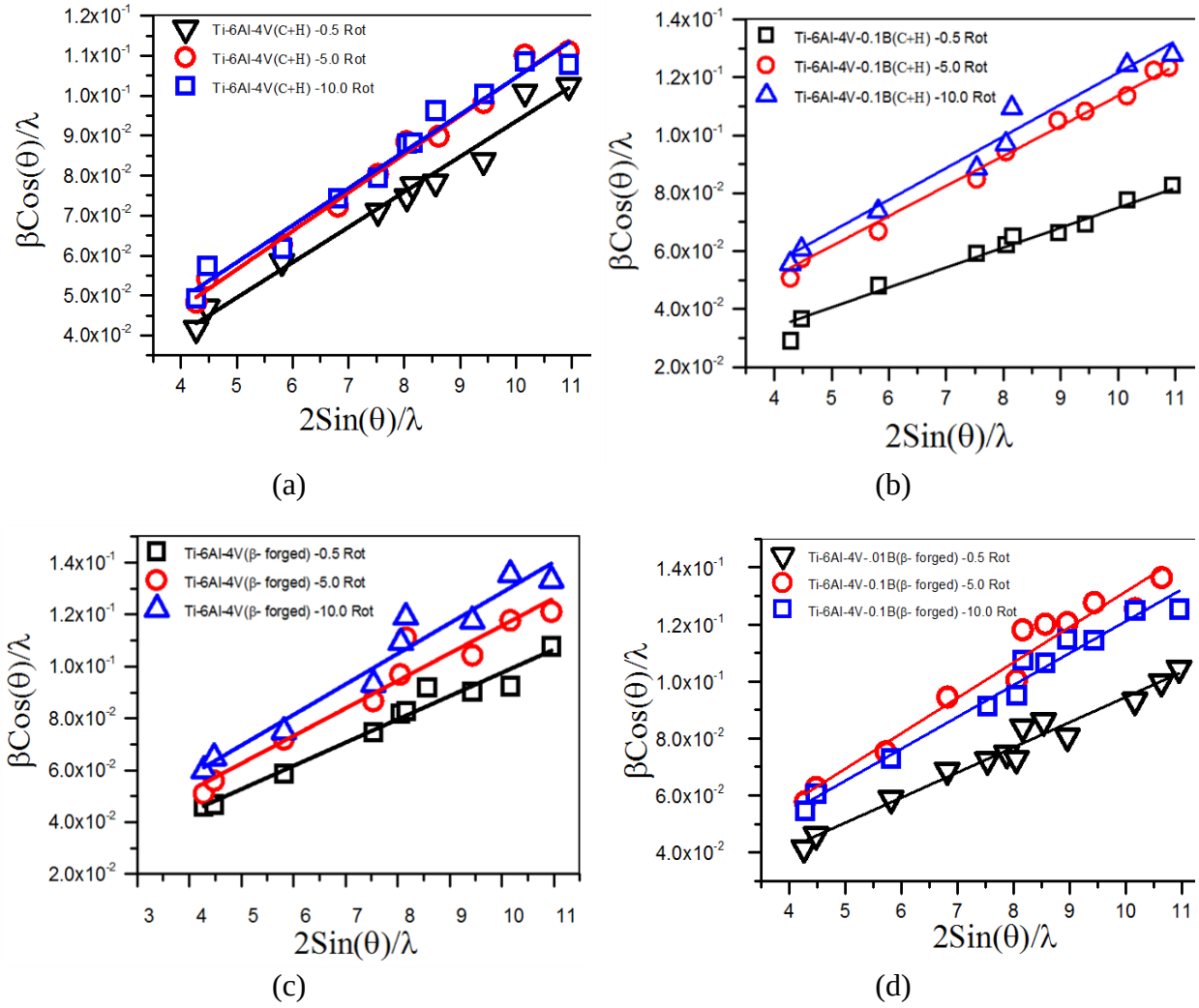

Supplementary Figure S.3: Classical Williamson-Hall plot showing the variation in FWHM with HPT-rotations for (a), (b) Ti64-C and Ti64+B-C alloys, respectively, in as-cast condition and (c), (d) Ti64-F and Ti64+B-F alloys, respectively, in β-forged condition.

3.2. Convolute multiple whole profile fitting (CMWP) techniques

For information related to dislocation density, dislocation arrangement and strain anisotropy, convoluted multiple whole profile (CMWP) fitting can be used for the analysis of XRD data [7]. In this method, measured X-ray diffraction data is fitted with a theoretical profile generated by a combination of background spline plus the convolution of instrument pattern and profiles related to size, strain and planner defects. CMWP method is therefore based on the convolution of three functions [8]:

$$I_{meas} = I_S + I_d + I_{SF} + I_{Inst} + BG \quad \ldots\ldots\ldots\ldots\ldots\ldots\ldots\ldots (3)$$

where, I_{meas} is the measured X-ray profile, I_{Ins} is the instrument profile and BG is the background determined before fitting; I_S, I_d and I_{SF} are the functions related to size, contrast of dislocations and planar defects such as twins and stacking faults, respectively. CMWP fitting provides median (m) and logarithmic variance (σ) of log-normal size distribution function from which dislocation density (ρ), dislocation arrangement parameter (M), and twin density (β) can be calculated [7, 9]. The effective strain field of dislocations can also be calculated from the core cut-off radius (R_e) [10]. Representative CMWP fitting plots for the unmodified and Boron modified alloys in β-forged conditions after 0.5, 5 and 10 HPT-rotations are provided in **Supplementary Figures S.4a-f**. Further mathematical details about the CMWP fitting procedure are available elsewhere [9].

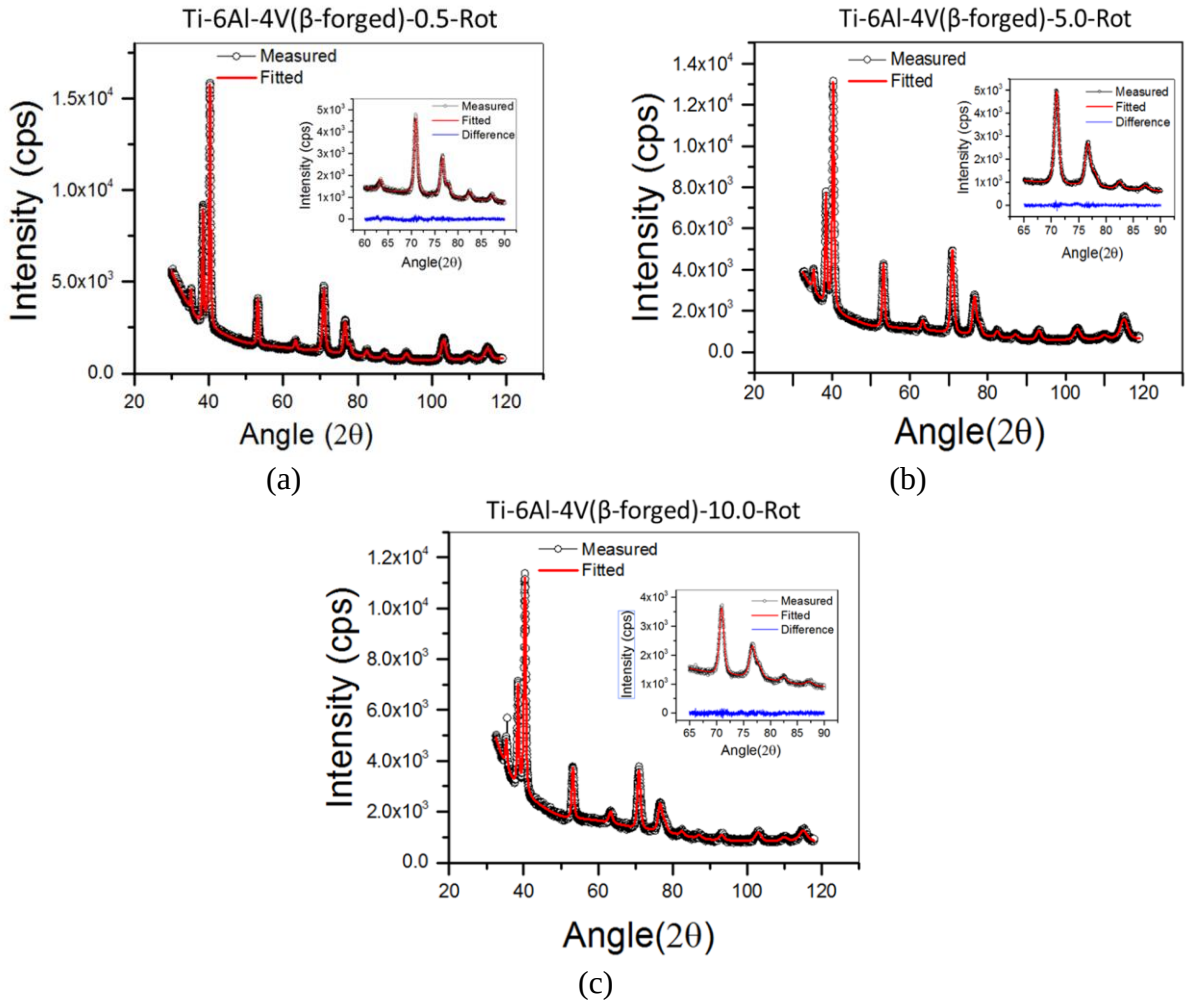

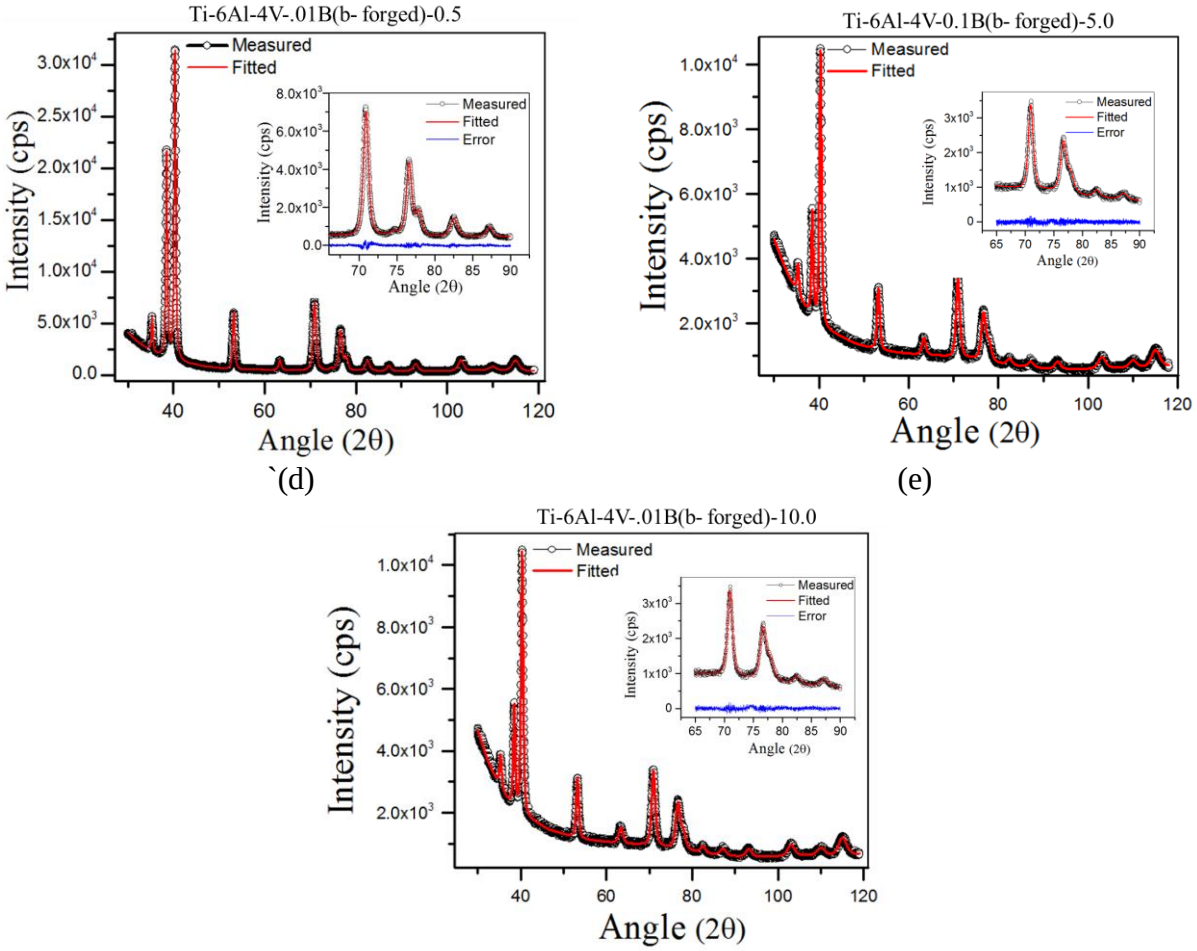

Supplementary Figure S.4: CMWP fitting of experimental XRD profile with the simulated one for (a), (b), (c) Ti64-F and (d), (e), (f) Ti64+B-F alloys in β-forged condition after 0.5, 5 and 10 HPT-rotations. The black and red lines correspond to measured and fitted patterns, respectively. Sections of measured and fitted XRD data are also shown in insets. The difference in intensity between measured and fitted patterns are shown by blue lines.

4. Standard stereographic triangle superimposed with reference color triangle for hcp materials

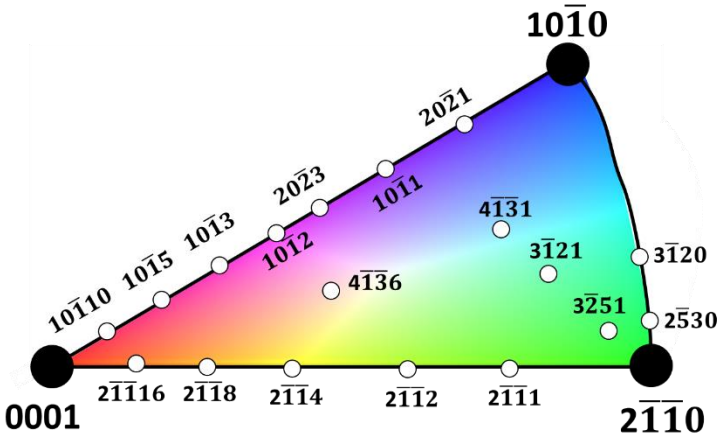

5. Strength modeling: Theory

The primary mechanisms of strength increment with increasing equivalent strain for HPT-processed alloys are Hall-Petch strengthening due to microstructural refinement and Taylor strengthening from increase in dislocation density. The resultant strength (yield strength) can be expressed from an appropriate summation law as [11]:

$$\sigma_{\text{calculated}} = (\sigma_o)^p + \left(\Delta\sigma_{\text{Taylor}}\right)^p + (\Delta\sigma_{\text{Hall-Petch}})^p \quad \ldots\ldots\ldots\ldots\ldots\ldots\ldots\ldots(2)$$

where σ_o is the inherent strength of the alloy, $\Delta\sigma_{\text{Taylor}}$ and $\Delta\sigma_{\text{Hall-Petch}}$ are strength increment due to Talor and Hall-Petch strengthening contributions, respectively. The summation coefficient, p varies between 1 (no overlap between contributing factors) and 2 (significant overlap between one or more of the contributing factors). A linear summation law ($p = 1$) is generally applicable when individual strengthening components originates from "strong" or long-range obstacles (e.g. grain boundary, precipitates and/or dispersion strengthening etc.) to dislocation motion [12, 13]. On the other hand, p varies between 1 and 2 (most often 1.5) due to "weak or short range" (e.g. solute atoms) obstacles causing strengthening. In case of SPD-processed Titanium alloys, contributions from various strengthening mechanisms ($\Delta\sigma_{\text{Taylor}}$ and $\Delta\sigma_{\text{Hall-Petch}}$) to the overall strength increment is not quite well understood and several different approaches have been adopted previously [14-17]. Considering linear summation ($p = 1$), final form of $\sigma_{\text{calculated}}$ is given as:

$$\sigma_{\text{calculated}} = \sigma_o + \Delta\sigma_{\text{Taylor}} + \Delta\sigma_{\text{Hall-Petch}} = \sigma_o + \alpha GMb\sqrt{\rho} + \frac{K}{\sqrt{d}} \quad \ldots\ldots\ldots\ldots \quad (3)$$

Here $\sigma_o = 440$ GPa is the internal friction stress for Ti-6Al-4V alloy [18]; α is a constant related to the arrangement of dislocations; $G = 44$ GPa is the shear modulus for Ti-6Al-4V-0.1B alloy [19]; $M = 3$ is the Taylor factor; $\vec{b} = 0.295$ nm is the Burgers vector for $\frac{a}{2} < 11\bar{2}0 >$ dislocations of hcp α-Ti [15]; ρ is the dislocation density; K is the Hall-Petch constant and d is the grain size equivalent to the crystallite size in the present case [20, 21]. Both ρ and d corresponding to various equivalent strains are obtained from CMWP analysis (**Figure 8** in the main manuscript). K and α are varied as a free parameter in strength modeling. The measured yield strength (σ_{measured}) is determined from measured hardness values (**Figure 9a** in the main manuscript) using empirical relationship [22]:

$$\sigma_{\text{measured}} = 2.26 \times (HV)_{\text{measured}} \quad \ldots\ldots\ldots\ldots\ldots\ldots (4)$$

where σ_{measured} is the yield stress in MPa, and $(HV)_{\text{measured}}$ is the Vickers hardness number. The hardness values correspond to equivalent strain or number of HPT-rotations for which ρ and d calculations were carried out by CMWP analysis.

The linear summation for $\sigma_{\text{calculated}}$ often leads to an overestimation of measured strength for SPD-processed materials with refined (sub-micron) microstructures [15]. This discrepency can be corrected by either reducing K-parameter alone or independently refining both K and α values based on microstructural information. To do this, Marquard-Levenberg nonlinear fitting is adopted in the present study where the sum of the square of ($\sigma_{\text{measured}} - \sigma_{\text{calculated}}$) are minimized with respect to various combinations of K and α parameters [23]. As shown in **Supplementary Figure S.5**, K and α values, which produce minimum sum of the square of ($\sigma_{\text{measured}} - \sigma_{\text{calculated}}$) are indeed unique.

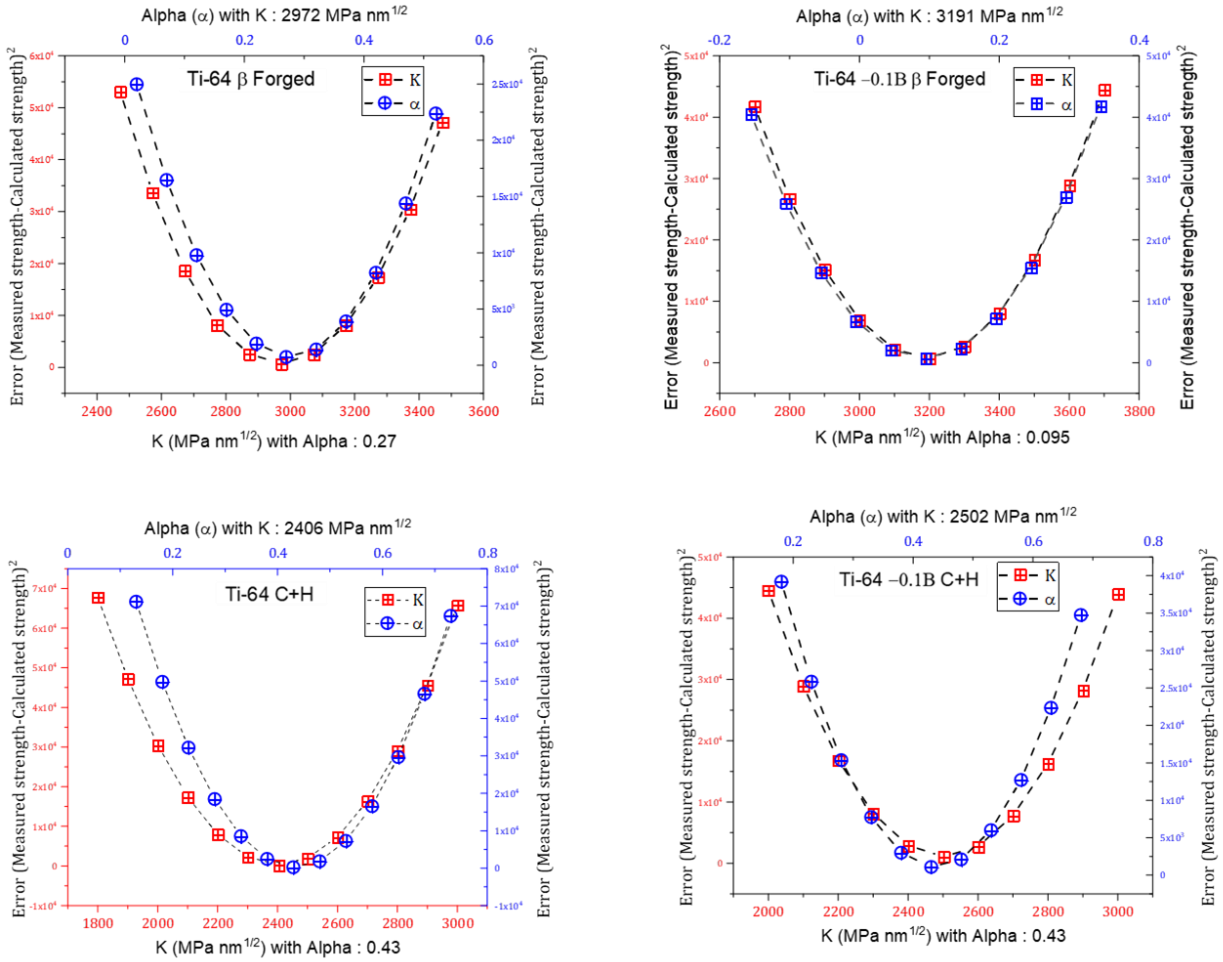

Supplementary Figure S.5: Marquard-Levenberg nonlinear fitting for minimum sum of the square of $(\sigma_{\text{measured}} - \sigma_{\text{calculated}})$ with respect to various combinations of K and α parameters.

References:

[1] B.D. Cullity, Elements of X-ray Diffraction, Addison-Wesley, Reading, MA, USA 1978.

[2] G. Williamson, W. Hall, X-ray line broadening from filed aluminium and wolfram, Acta Metallurgica 1(1) (1953) 22-31.

[3] D. Balzar, H. Ledbetter, Voigt-function modeling in Fourier analysis of size- and strain-broadened X-ray diffraction peaks, Journal of Applied Crystallography 26(1) (1993) 97-103.

[4] A.R. Stokes, A Numerical Fourier-analysis Method for the Correction of Widths and Shapes of Lines on X-ray Powder Photographs, Proceedings of the Physical Society 61(4) (1948) 382.

[5] T. Ungár, A. Borbély, The effect of dislocation contrast on x-ray line broadening: A new approach to line profile analysis, Applied Physics Letters 69(21) (1996) 3173-3175.

[6] A. Sarkar, S. Roy, S. Suwas, X-ray diffraction line profile analysis of deformation microstructure in boron modified Ti–6Al–4V alloy, Materials Characterization 62(1) (2011) 35-42.

[7] G. Ribárik, T. Ungár, J. Gubicza, MWP-fit: a program for multiple whole-profile fitting of diffraction peak profiles by ab initio theoretical functions, Journal of Applied Crystallography 34(5) (2001) 669-676.

[8] G. Ribarik, T. Ungar, J. Gubicza, MWP-fit: a program for multiple whole-profile fitting of diffraction peak profiles by ab initio theoretical functions, Journal of Applied Crystallography 34(5) (2001) 669-676.
[9] G. Ribárik, J. Gubicza, T. Ungár, Correlation between strength and microstructure of ball-milled Al–Mg alloys determined by X-ray diffraction, Materials science and engineering: A 387 (2004) 343-347.
[10] M. Wilkens, The determination of density and distribution of dislocations in deformed single crystals from broadened X-ray diffraction profiles, Physica status solidi (a) 2(2) (1970) 359-370.
[11] S. Roy, L.F. Allard, A. Rodriguez, W.D. Porter, A. Shyam, Comparative Evaluation of Cast Aluminum Alloys for Automotive Cylinder Heads: Part II—Mechanical and Thermal Properties, Metall and Mat Trans A 48(5) (2017) 2543-2562.
[12] A. de Vaucorbeil, W.J. Poole, C.W. Sinclair, The superposition of strengthening contributions in engineering alloys, Materials Science and Engineering: A 582 (2013) 147-154.
[13] A.W. Zhu, A. Csontos, E.A. Starke Jr, Computer experiment on superposition of strengthening effects of different particles, Acta Materialia 47(6) (1999) 1713-1721.
[14] G.S. Dyakonov, S. Mironov, I.P. Semenova, R.Z. Valiev, S.L. Semiatin, Microstructure evolution and strengthening mechanisms in commercial-purity titanium subjected to equal-channel angular pressing, Materials Science and Engineering: A 701 (2017) 289-301.
[15] Y.G. Ko, D.H. Shin, K.-T. Park, C.S. Lee, An analysis of the strain hardening behavior of ultra-fine grain pure titanium, Scripta Materialia 54(10) (2006) 1785-1789.
[16] M.T. Jia, D.L. Zhang, B. Gabbitas, J.M. Liang, C. Kong, A novel Ti–6Al–4V alloy microstructure with very high strength and good ductility, Scripta Materialia 107 (2015) 10-13.
[17] P. Luo, D.T. McDonald, S.M. Zhu, S. Palanisamy, M.S. Dargusch, K. Xia, Analysis of microstructure and strengthening in pure titanium recycled from machining chips by equal channel angular pressing using electron backscatter diffraction, Materials Science and Engineering: A 538 (2012) 252-258.
[18] Z.X. Zhang, S.J. Qu, A.H. Feng, J. Shen, Achieving grain refinement and enhanced mechanical properties in Ti–6Al–4V alloy produced by multidirectional isothermal forging, Materials Science and Engineering: A 692 (2017) 127-138.
[19] I. Sen, U. Ramamurty, Elastic modulus of Ti–6Al–4V–xB alloys with B up to 0.55wt.%, Scripta Materialia 62(1) (2010) 37-40.
[20] U.F. Kocks, H. Mecking, Physics and phenomenology of strain hardening: the FCC case, Progress in Materials Science 48(3) (2003) 171-273.
[21] N. Hansen, Hall–Petch relation and boundary strengthening, Scripta Materialia 51(8) (2004) 801-806.
[22] Y.L. Shen, N. Chawla, On the correlation between hardness and tensile strength in particle reinforced metal matrix composites, Materials Science and Engineering: A 297(1) (2001) 44-47.
[23] K. Levenberg, A METHOD FOR THE SOLUTION OF CERTAIN NON-LINEAR PROBLEMS IN LEAST SQUARES, Quarterly of Applied Mathematics 2(2) (1944) 164-168.